https://doi.org/10.5194/egusphere-2025-5020
Preprint. Discussion started: 16 October 2025

Spatiotemporal patterns in CO_2 fluxes and geochemical weathering in mountain glacial rivers

Jessica A. Serbu[1,2] (ORCID 0000-0002-0109-4550),
Suzanne E. Tank[1] (ORCID 0000-0002-5371-6577),
Bernhard Peucker-Ehrenbrink[2] (ORCID 0000-0002-3819-992X),
Xiying Sun[3] (ORCID 0009-0004-5759-4425)
Craig A. Emmerton[1] (ORCID 0000-0001-9511-9191)
Vincent L. St.Louis[1] (ORCID 0000-0001-5405-1522)

[1]Department of Biological Sciences, University of Alberta, Edmonton, AB, Canada
[2]Marine Chemistry and Geochemistry Department, Woods Hole Oceanographic Institution, Woods Hole, MA, USA
[3]Department of Oceanography, Texas A&M University, College Station, TX, USA

Corresponding author: Jessica Serbu (serbu@ualberta.ca)

Abstract

Despite low temperatures that slow chemical reactions, geochemical weathering can be pronounced in glacial rivers due to large quantities of fresh comminuted sediments (glacial flour). We assessed the types and magnitude of geochemical weathering across multiple seasons and years in three proglacial rivers (Sunwapta-Athabasca, North Saskatchewan, and Bow) on the eastern slopes of the Canadian Rocky Mountains, as they meandered from their alpine glacial origins to the montane altitudinal life zone up to 100 kms downstream. To overcome the inherent ecological complexity of our study region, multiple lines of evidence were used to quantify geochemical weathering along river transects and across seasons. Carbon dioxide (CO_2) was highly undersaturated and instantaneous CO_2 fluxes mostly net consumptive at sampling sites nearest source glaciers. Basic geochemical parameters and a large suite of isotopes ($^{87}Sr/^{86}Sr$, $\delta^{34}S$-SO_4, $\delta^{18}O$-SO_4, $\delta^{13}C$-PIC, $\delta^{13}C$-DIC, and $\Delta^{14}C$-DIC) were used to dissect general trends in weathering geochemistry. These trends were supported by an inversion model and an inorganic-organic carbon mass balance model, which together found that while carbonate weathering dominated at all

https://doi.org/10.5194/egusphere-2025-5020
Preprint. Discussion started: 16 October 2025

sampling sites and times, silicate weathering and organic carbon contributions to the dissolved inorganic carbon pool increased with distance downriver of glaciers regardless of season. Globally, we suspect these spatiotemporal patterns in the type and magnitude of geochemical weathering are common across glacierized watersheds. Therefore, as glaciers continue to retreat, we can expect to see an encroachment of downriver altitudinal life zones concurrent with glacier mass loss and an evolution of in-river geochemical weathering processes, with direct implications for present-day regional and global carbon budgets.

Short summary

In water, CO_2 can chemically react with (i.e., weather) fine sediment produced as glaciers abrade bedrock. Studying three glacier-fed rivers in the Canadian Rockies across multiple seasons, we found that near glaciers, rivers consumed CO_2 mainly via carbonate weathering. Importance of silicate weathering and organic matter decomposition as drivers of CO_2 cycling increased downriver. As glaciers retreat, subsequent shifts in river biogeochemistry will affect regional and global carbon budgets.

1 Introduction

Geochemical weathering plays an important role in local (Kempe, 1988) to global (Isson et al., 2020) carbon cycling. However, the direction and magnitude of the effect on the carbon cycle depends on both the source of protons and the minerals they act upon (S.-L. Li et al., 2008; Viers et al., 2007). For instance, carbonate weathering by carbonic acid consumes one mole of CO_2 for every mole of carbonate mineral (Eq. 1) (Mackenzie & Garrels, 1966; Martin, 2017; Meybeck, 1993; Rubey, 1951; Urey, 1952). This is significant because carbonates are easily weatherable minerals compared to many rock-forming silicates, and often dominate weathering reactions, even when carbonates are present in minor amounts (Blum et al., 1998). However, carbonate weathering is atmospheric CO_2 net neutral on geological timescales (Eq. 2) (Liu et al., 2011). Consequently, many studies focus on silicate weathering (Eq. 3) and sulfide oxidation-carbonate dissolution (Eq. 4), which are net consumers and emitters of CO_2, respectively (Berner, 1992; Torres et al., 2017; Walker et al., 1981). Hence, spatiotemporal quantification of all forms of geochemical weathering

https://doi.org/10.5194/egusphere-2025-5020
Preprint. Discussion started: 16 October 2025

is crucial to determining accurate present-day regional CO_2 budgets (Khadka et al., 2014; St. Pierre et al., 2019) and our full understanding of the global carbon cycle (Donnini et al., 2016; Robison et al., 2023).

$$CaCO_{3(s)} + H_2O + CO_{2(g)} \rightarrow Ca^{2+} + 2HCO_3^- \quad \textbf{(Eq. 1)}$$

$$Ca^{2+} + 2HCO_3^- \rightarrow CaCO_{3(s)} + H_2O + CO_{2(g)} \quad \textbf{(Eq. 2)}$$

$$CaAl_2Si_2O_{8(s)} + 3H_2O + 2CO_{2(g)} \rightarrow Ca^{2+} + 2HCO_3^- + Al_2Si_2O_5(OH)_{4(s)} \quad \textbf{(Eq. 3)}$$

$$4FeS_2 + 15O_2 + 14H_2O \rightarrow 4Fe(OH)_3 + 8H_2SO_4$$

$$CaCO_3 + H_2SO_4 \rightarrow CO_{2(g)} + H_2O + Ca^{2+} + SO_4^{2-} \quad \textbf{(Eq. 4)}$$

The magnitude of geochemical weathering in glacierized watersheds has been shown to surpass the global mean, in part due to the high discharge associated with glacial melt (S. P. Anderson et al., 1997; Sharp et al., 1995). Geochemical weathering in glacierized watersheds is supported by heightened physical weathering of bedrock in subglacial environments (S. P. Anderson et al., 2000; Sharp et al., 1995; St. Pierre et al., 2019) that produces fine-grained comminuted sediments (glacial flour) with high surface area:volume ratios (Raiswell, 1984) and low weathering maturity (Deuerling et al., 2019). Once transport in meltwater discharge removes these sediments from the cold temperatures and restricted atmospheric exposure of subglacial environments (Tranter & Wadham, 2014), their potential for chemical weathering increases (S. P. Anderson et al., 2000). Yet, most research thus far on geochemical weathering in glacial systems has been conducted subglacially (Graly et al., 2014; X. Li et al., 2022; Tranter et al., 2002), in immediate proglacial environments (Hodson et al., 2000; Sharp et al., 1995; Urra et al., 2019), or over summer field campaigns when sampling sites were accessible (Deuerling et al., 2019; Scribner et al., 2015; St. Pierre et al., 2019). Despite glaciers serving as hotspots of chemical weathering globally, we still know little about how the type and magnitude of various geochemical weathering reactions persist downriver, and how this effect may change seasonally or interannually.

The goals of this study were to quantify changing types and extent of geochemical weathering spatiotemporally along three proglacial rivers in Jasper and Banff National Parks on the eastern slopes of the Canadian Rocky Mountains. This mid-latitude alpine region is home to small warm-based glaciers with moderate discharge and sediment transport potentials. River transects were

https://doi.org/10.5194/egusphere-2025-5020
Preprint. Discussion started: 16 October 2025

established from 0.2 km below the glacier tongue, through alpine, subalpine, and montane altitudinal life zones up to 100 km downstream, with the underlying ecological complexity shaping our geochemical study. To overcome this complexity, multiple lines of evidence were used to assess the type and magnitude of geochemical weathering as one moved downriver and temporally. First, instantaneous carbon dioxide (CO_2) fluxes were calculated to determine the amount of net consumption or emission of CO_2 between our study rivers and the atmosphere. Second, we assessed basic river geochemistry and a large suite of isotopes ($^{87}Sr/^{86}Sr$, $\delta^{34}S$-SO_4, $\delta^{18}O$-SO_4, $\delta^{13}C$-PIC, $\delta^{13}C$-DIC, and $\Delta^{14}C$-DIC) to investigate trends in weathering that occurred along our study rivers and across seasons. Using some of that chemistry, we then applied an inversion weathering model to determine the proportion of ions derived from precipitation, evaporite, carbonate, silicate, and pyrite endmembers (Kemeny & Torres, 2021). Finally, an inorganic-organic carbon mass balance model was used to estimate the proportions of riverine dissolved inorganic carbon (DIC) that resulted from carbonate weathering and the atmosphere, respiration of organic carbon (OC), and silicate weathering (Voss et al., 2023) in these ecologically complex river systems. Using these lines of evidence, we show that carbonate weathering dominated at all sites and throughout all seasons, but that OC and silicate weathering contributions to the DIC pool increased moving downriver from glacierized alpine to montane altitudinal life zones.

2 Methods

2.1 Study region

The headwater regions of the Sunwapta, Athabasca, North Saskatchewan, and Bow rivers are contained within the montane cordillera ecozone and span alpine, subalpine, and montane altitudinal life zones (Demuth & Horne, 2017). In total, we established seven sampling sites along the Sunwapta-Athabasca River continuum, three sampling sites along the North Saskatchewan River, and four sampling sites along the Bow River (**Figure 1A**; **Table S1**).

https://doi.org/10.5194/egusphere-2025-5020
Preprint. Discussion started: 16 October 2025

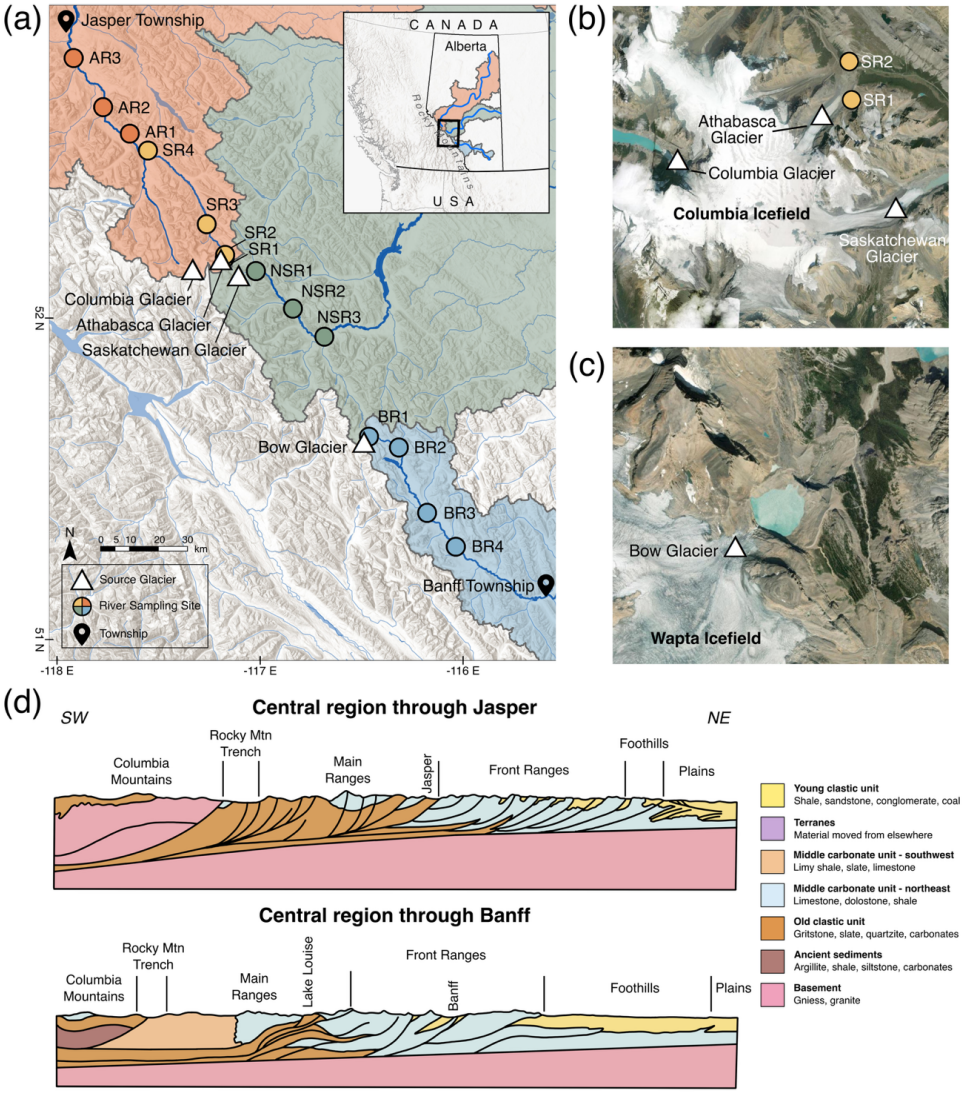

Figure 1. (A) Map of source glaciers and our sampling sites on the Sunwapta (SR), Athabasca (AR), North Saskatchewan (NSR), and Bow (BR) rivers. Sampled watersheds are color-coded and match the watersheds depicted on the inset map of Alberta, Canada. All sampling was conducted in the headwaters of these major river systems in Jasper and Banff National Parks (Park boundaries not shown). Modified from Serbu, St. Louis, et al., 2024. (B) The Columbia Icefield. (C) The Wapta Icefield. (D) Geological cross-sections of the Canadian Rocky Mountains near Jasper (top) and Banff (bottom), reproduced from Gadd (2009) with permission. Map and image (A-C) credits are: Location pin by Sophie Haskind (CC BY 3.0); Service Layer Credits: World Imagery: Earthstar Geographics; World Imagery: Maxar World Hillshade: Esri, USGS; World Topographic Canadian Style: Esri, TomTom, Garmin, FAO, NOAA, USGS, EPA, NRCan, Parks Canada; World Hillshade: Esri, CGIAR, USGS.

https://doi.org/10.5194/egusphere-2025-5020
Preprint. Discussion started: 16 October 2025

2.1.1 Site descriptions

The Athabasca Glacier, a valley glacier of the Columbia Icefield (**Figure 1B**), is the point of origin for the Sunwapta River (SR sites; Ommanney, 2002). The Sunwapta River passes through a proglacial lake prior to braiding through a sparsely vegetated glacial outwash plain. The braids converge into one channel and further downriver merge into the Athabasca River (AR sites), which originates upriver of this juncture at the Columbia Glacier in the northwest margin of the Columbia Icefield (**Figure 1B**) (Ommanney, 2002). The large Athabasca River flows northeast towards our most northerly sampling site 97.8 km downriver, upriver of Jasper Township (**Figure 2**).

The North Saskatchewan River (NSR sites) originates at the Saskatchewan Glacier on the southern edge of the Columbia Icefield (**Figure 1B**) (Ommanney, 2002). Meltwaters from the Saskatchewan Glacier, the largest outlet glacier of the Columbia Icefield, terminate into a large proglacial lake before flowing downriver through a glacial valley. From there, the North Saskatchewan River meanders through a prominent glacial floodplain area vegetated with low-lying shrubs and grasses before forming a single large channel that flows through montane forest until our last sampling site 46.3 km downriver (**Figure 2**).

The Bow River (BR sites) begins at the cirque Bow Glacier in the Wapta Icefield (**Figure 1C**) (Ommanney, 2002), flowing from proglacial Iceberg Lake, over a large waterfall, and into a braided forefield. The Bow River then feeds Bow Lake, a large subalpine lake surrounded by subalpine forest, before it passes through a forested wetland area. Dense montane forest lines the remainder of the headwaters of the Bow River towards our most southerly sampling site 75.4 km downriver, upriver of Banff Township (**Figure 2**).

https://doi.org/10.5194/egusphere-2025-5020
Preprint. Discussion started: 16 October 2025

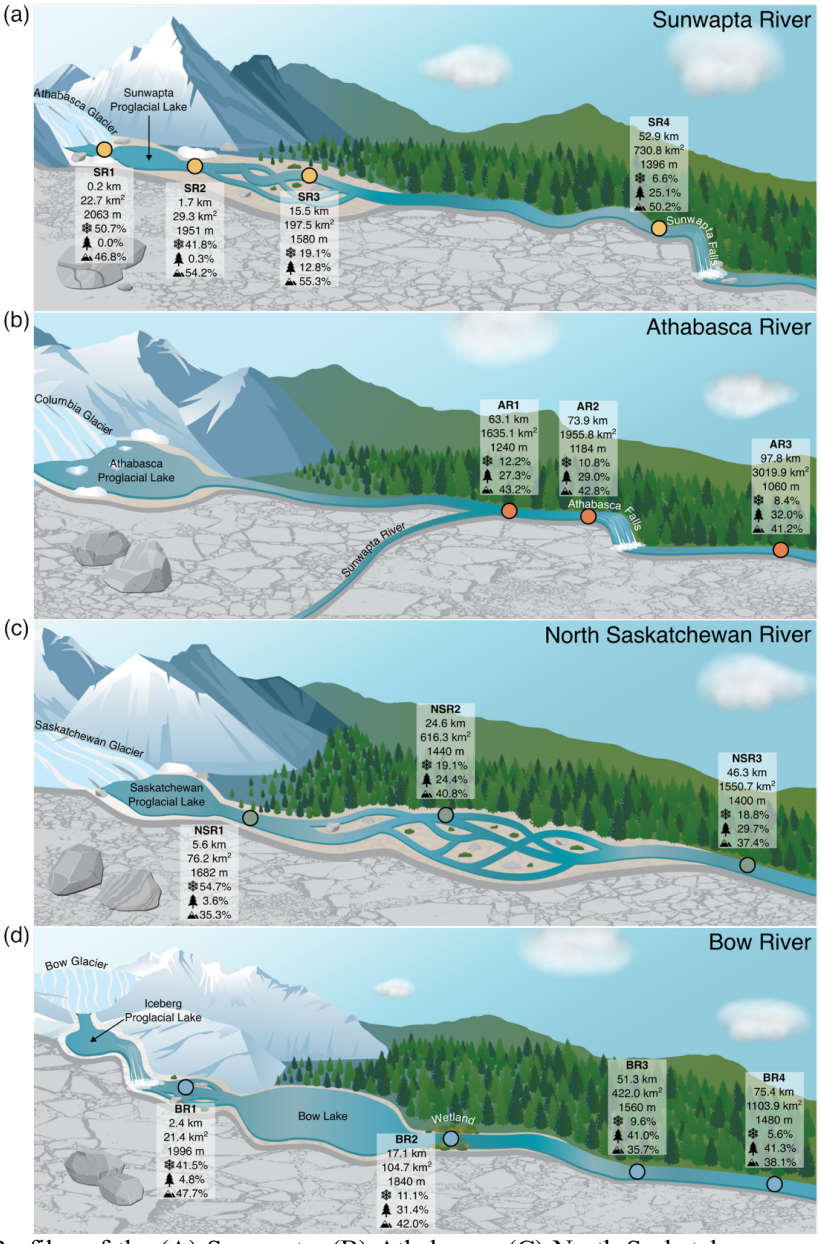

Figure 2. Profiles of the (A) Sunwapta, (B) Athabasca, (C) North Saskatchewan, and (D) Bow rivers with sampling sites, distance from glacier, watershed area, elevation, and notable river features included. Relative percent watershed area covered by major land cover classes in our study system (snow and ice [snowflake], coniferous forest [tree], and rock and rubble [mountain]) are listed for each site. For further site descriptions, including river abbreviations, exact sampling locations, and relative percent land covered by minor land cover classes, please see **Table S1** and **Table S2**. Distances and elevations are not precisely to scale. Reproduced from Serbu, St. Louis, et al., 2024.

https://doi.org/10.5194/egusphere-2025-5020
Preprint. Discussion started: 16 October 2025

2.1.2 Geology

Our sampling sites in the central region of the eastern slopes of the Canadian Rocky Mountains are underlain by a Lower Cambrian coarse clastic unit, comprised of quartzite, siltstone, and limestone, and alternating Middle to Upper Cambrian fine clastic and carbonate units, comprised of limestone, shale, and siltstone, and limestone, dolostone, siltstone, and shale, respectively (**Figure S1**) (Gadd, 2009). Cross-sections of the mountain geology at Jasper and Banff indicate that the primary geology of the region is limestone, dolostone, and shale (**Figure 1D**).

More precisely, the Columbia Icefield sits atop Middle Cambrian limestone, dolostone, and shale formations (Pana & Elgr, 2013; Price, 2000). The Sunwapta River is in contact with the Upper Cambrian Lynx Group consisting of limestone and dolostone beds with siltstone at upriver sites, and the Lower Cambrian Gog Formation of limestone and dolostone alternating with siltstone at downriver sites (Mountjoy, 1962; Pana & Elgr, 2013). Downriver of where the Sunwapta River joins the Athabasca River, the Neoproterozoic Miette Group consisting of slate, schist, and gritstone is present (Pana & Elgr, 2013; Price, 2000). Across the North Saskatchewan River watershed, limestone dominates with some dolostone, chert, argillite, and quartzites (Pana & Elgr, 2013). The Wapta Icefield is underlain by formations of the Middle Cambrian and the Lower Cambrian Gog Group, all of which are comprised of primarily limestone, with some dolostone and quartzose sandstones (Mountjoy, 1962). Downriver, the Bow River is predominantly underlain by the Neo-Proterozoic Miette Group but is secondarily lined by various Middle Cambrian formations of limestone and dolomitic sandstones and the Lower Cambrian Gog Group (**Figure S1**) (Pana & Elgr, 2013).

2.1.3 Land cover class

For each sampling site, the relative percent of watershed area covered by major and minor land cover classes was determined with the Alberta Biodiversity Monitoring Institute (ABMI) Wall-to-Wall Land Cover Inventory and the relative percent of its watershed area covered by wetland type was determined with the ABMI Wetland Inventory (**Table S2**) (Alberta Biodiversity Monitoring Institute, 2010, 2021). Of the 10 land cover classes, only three (snow and ice, rock and rubble, and

https://doi.org/10.5194/egusphere-2025-5020
Preprint. Discussion started: 16 October 2025

coniferous forest) exceeded 10 % cover of the watershed area at some of our sampling sites. Other land cover classes pertaining to diverse vegetation (e.g., grassland, broadleaf forest) or anthropogenic disturbance (i.e., developed, including roads) represented less than 10 % of the land cover along our sampling reaches, highlighting the barren and pristine landscape of our study region. Intuitively, the relative percentage of cumulative watershed area covered by snow and ice was highest at our sampling sites nearest glaciers (41.5 – 54.7 %), whereas the relative percentage of cumulative watershed area covered by coniferous forest was highest (29.7 – 41.3 %) at our most distant sampling sites on each river. The proportion of cumulative watershed area covered by rock and rubble was relatively constant (35.7 – 55.3 %) across river reaches, but slightly higher at the glacial outwash floodplain sites (**Figure 2**, **Table S2**).

2.2 River discharge

Measured and modeled discharge data for each sampling site were previously detailed by Serbu, St. Louis, et al. (2024) (**Figure S2**). Briefly, mean daily river discharge (m^3 s^{-1}) was directly quantified at two of our 14 sampling sites (SR2 and BR3) by hydrometric gauging stations maintained by Water Survey of Canada (WSC; Water Survey of Canada, 2021). To estimate daily discharge at the remaining 12 sampling sites, we used day-specific watershed area-discharge linear regression models derived from mean daily discharge measured at nine Albertan mountain river WSC hydrometric gauging stations (**Table S3**, **Figure S2**). More specifically, we downloaded WSC measured discharge from the nine gauging stations and created simple daily linear regressions for 2019 and 2020 (i.e., 730 linear regressions) before applying the linear regression equations to the watershed areas for each sampling site and for each day of the year(s). The nine WSC gauging stations, including those at our sampling sites SR2 and BR3, were selected because they were all within the Sunwapta-Athabasca, North Saskatchewan, and Bow watersheds, had watershed areas similar to those of our sampling sites, and were operational during our river sampling years of 2019 and 2020. Watershed areas for our sampling sites were obtained directly from WSC (SR2 and BR3) or delineated using the Alberta ArcHydro Phase 2 Dataset on ArcGIS (all other sites; Alberta Environment and Parks, 2018).

2.3 Sample collection and analyses

https://doi.org/10.5194/egusphere-2025-5020
Preprint. Discussion started: 16 October 2025

2.3.1 Sample collection

Sampling sites were visited monthly in 2019 and 2020 during the open water season, beginning during snowmelt in late May/early June, through peak glacial melt in July/August, then during the receding flow period in September/October (**Figure S2**) (Serbu, St. Louis, et al., 2024). Due to safety concerns of sampling fast flowing rivers in remote areas, all sample collection was conducted near shorelines in the main flow of rivers. However, turbulence and mixing are high in this steep-slope region, and back-eddies, slumping shorelines, and areas where in-river sediment could be disturbed were strictly avoided, ensuring a representative sample. In braided river sections (i.e., SR3 and NSR2), the main channel was selected for sample collection. Additional samples were collected twice in winter (December 2019, January 2021) during base flow, but only at sites that were partially ice free and safe to sample when harnessed in.

In situ parameters

At each river sampling site and time, we deployed a YSI Inc. EXO2 multiparameter sonde to obtain instantaneous measures of optical dissolved oxygen (ODO; % saturation and concentration), conductivity, turbidity, pH, and temperature. Sondes were factory serviced annually prior to spring fieldwork, and sensors calibrated prior to each sampling campaign except for ODO, which was calibrated at each sampling site and time. Low ionic strength standards were not used for the calibration of pH or conductivity, and as a result, possible measurement biases may have occurred in our low ionic glacial meltwaters (Bagshaw et al., 2021). However, we calibrated often, opted for spot sampling over long term deployments, and eliminated the first five minutes of data at each site ensuring in situ equilibrium was reached, all of which help to reduce bias (Bagshaw et al., 2021). Sonde data was used to support the collected geochemistry samples during data analysis.

Atmospheric $CO_{2(g)}$ and dissolved in situ riverine $CO_{2(aq)}$ concentrations were measured to calculate percent saturation and model instantaneous CO_2 fluxes. $CO_{2(g)}$ and $CO_{2(aq)}$ concentrations were directly measured with a Vaisala CARBOCAP® GM70 Hand-Held CO_2 Meter fitted with a 0 – 2000 ppm GMP222 CO_2 probe. All CO_2 probes underwent certified factory calibration

https://doi.org/10.5194/egusphere-2025-5020
Preprint. Discussion started: 16 October 2025

annually, but were also checked inhouse against Praxair 47.9, 347 and 910 ppm certified CO_2 standards both before and after field seasons. Temperature (T) (air T for $CO_{2(g)}$ and water T for $CO_{2(aq)}$ readings) and true barometric pressure (non-sea level corrected) were input into the Vaisala meter at each sampling site and time. Atmospheric $CO_{2(g)}$ concentrations were measured by suspending the probe ~1 meter above ground in a clearing back from the edge of the river. CO_2 probes used to quantify dissolved $CO_{2(aq)}$ concentrations were encased within a tight fitting waterproofing polytetrafluoroethylene (PTFE) sleeve permeable to gas exchange (M. S. Johnson et al., 2010). These probes were then deployed into the main current of the river just below the surface. To further assess the accuracy of these $CO_{2(aq)}$ measurements, we on one occasion tested them against $CO_{2(aq)}$ concentrations measured using a gas displacement technique and a PP Systems EGM-5 Portable CO_2 Gas Analyzer as described by Zolkos et al., 2018; all measurements from the two methods were within ± 10 ppm. Measurements were conducted during the daytime when weathering and photosynthesis were theoretically at their peak, so $CO_{2(aq)}$ concentrations may be biased low, when compared to a daily mean (de Montety et al., 2011).

Elemental and isotope geochemistry

Water samples for major cation (Ca^{2+}, K^+, Mg^{2+}, Na^+) analyses were filtered onsite with all-plastic syringes and 0.45 µm Whatman™ polyethersulfone (PES) syringe filters into high density polyethylene (HDPE) scintillation vials, then preserved with trace metal grade HNO_3 until pH < 2 in our field laboratory within 12 hours of collection. All syringes and scintillation vials used for cation sampling and storage were first soaked in 0.01% CITRANOX® acid detergent overnight, followed by a 10 % HCl bath overnight, and rinsed thoroughly with Millipore Milli-Q™ water. Water collected for dissolved silica (Si) analyses was filtered onsite through a 0.45 µm Sartorius™ Minisart™ cellulose acetate syringe filters.

Concentrations of DIC and dissolved OC (DOC), along with their isotopic signatures, were quantified for use in the DIC mass balance model (detailed below), as well as to help place our samples in context with those measured in other global regions. Water samples collected for analyses of DIC, $\delta^{13}C$-DIC, and $\Delta^{14}C$-DIC analyses were processed at each sampling site using the same 0.45 µm Sartorius™ Minisart™ cellulose acetate syringe filter, then stored without

https://doi.org/10.5194/egusphere-2025-5020
Preprint. Discussion started: 16 October 2025

headspace in pre-washed and muffled glass Labco Exetainers® (DIC and δ^{13}C-DIC) or Wheaton bottles (Δ^{14}C-DIC) with rubber-lined caps. A known volume of water collected for particulate inorganic carbon (PIC) and δ^{13}C-PIC analyses was passed through a muffled and pre-weighed 25 mm 0.7 µm Whatman™ glass fiber filter (GF/F) within 12 hours of collection in our field laboratory, then frozen. Sampling protocols for particulate and dissolved OC (POC and DOC, respectively) and their respective isotopes were collected for a sister project and are detailed in Drapeau et al., 2025b. Briefly, water samples for DOC and δ^{13}C-DOC analyses were filtered onsite through a pre-washed 0.45 µm Basix™ PES filter into acid-washed and muffled amber glass receivers, while water samples for organic radiocarbon were transported back to the field laboratory and processed in glass filter towers cleaned the same way. Muffled and pre-weighed Whatman™ 0.7 µm GF/F filters were used to capture δ^{13}C-POC and Δ^{14}C-POC samples, and the filtrate from the latter was kept for analyses of Δ^{14}C-DOC. All DOC samples were preserved with trace metal grade HCl to 0.1 % of its volume, while POC filters were frozen in our field laboratory.

Water samples for analyses of anions (Cl^-, SO_4^{2-}), sulfate isotopes (δ^{34}S-SO_4, δ^{18}O-SO_4), and radiogenic strontium ($^{87}Sr/^{86}Sr$) analyses were filtered through a 47 mm 0.45 µm cellulose acetate filter in a pre-cleaned filtration tower in the field laboratory. Cation and anion concentrations were collected for use in the inverse weathering model and DIC mass balance, both described below. Sulfate isotopes were also collected for use in the inversion model, as well as for putting our data in context with those measured in other global regions. Radiogenic strontium was originally quantified to define the most appropriate carbonate and silicate endmembers in our system for a mass balance of DIC sources. However, we ultimately decided that $^{87}Sr/^{86}Sr$ ratios were not suitable to use as endmembers for the mass balance of DIC because our study region did not have lithological contrast like some regions (e.g., Muñoz et al., 2024). Instead, we describe $^{87}Sr/^{86}Sr$ ratios that were observed in our system. All water samples were stored in the dark at 4 °C until analysis.

Minerology

Finally, at each sampling site and time, a Geotech barrel filter holder was outfitted with 102 mm 0.45 µm Sterlitech PES filters and filled repeatedly with surface river water until filters were

https://doi.org/10.5194/egusphere-2025-5020
Preprint. Discussion started: 16 October 2025

clogged with particulates to determine the mineralogy of suspended sediment. The filters were then frozen.

2.3.2 Laboratory analyses

Elemental geochemistry

Major cations, anions, and Si were analyzed in the Canadian Association of Laboratory Accreditation (CALA)-accredited Biogeochemical Analytical Service Laboratory (BASL, University of Alberta). Major cations were analyzed on a Thermo Scientific iCAP 6300 Inductively Coupled Plasma – Optical Emissions Spectrometer (ICP-OES) using reference methods EPA 200.7 (U.S. EPA, 1994). Anions were analyzed on a Dionex DX-600 Ion Chromatography System following reference method EPA 300.1 (U.S. EPA, 1993), whereas Si was analyzed on a Lachat Instruments QuikChem® QC8500 FIA Automated Ion Analyzer using reference method SM 4500-SiO_2 (Standard Methods Committee of the APHA-a). An Apollo SciTech AS-C3 DIC Analyzer interfaced with a LI-COR Biosciences LI-7000 infrared CO_2 Analyzer was used to quantify DIC concentrations (Wang et al., 2017) while a Shimadzu Total Organic Carbon (TOC)-V Analyzer was used to quantify DOC concentrations (American Public Health Association et al., 2023b; Drapeau et al., 2025b).

Isotope geochemistry

δ^{13}C-DIC (2 SD = 0.3 ‰ VPDB) samples were first processed by converting all inorganic carbon to CO_2, followed by analysis on a Thermo Scientific Gasbench coupled to a Thermo Scientific DELTA V Plus Isotope Ratio (IR)-MS at the Environment Isotope Laboratory (EIL; University of Waterloo, Canada). Stable isotopes of SO_4^{2-} were also processed and quantified at the EIL, with prepared precipitations of δ^{34}S-SO_4 (2 SD = 0.3 ‰ VCDT) analyzed on a Costech Analytical Elemental Combustion System 4010 coupled to an Elementar isoprime presION IRMS. δ^{18}O-SO_4 (2 SD = 0.3 ‰ VSMOW) was analyzed via an Elementar vario PYRO Cube® Elemental Analyzer paired with a GV Instruments IsoPrime™ IRMS. δ^{13}C-PIC (2 SD = 0.05 ‰ VPDB) was quantified at the Ján Veizer Stable Isotope Laboratory (University of Ottawa, Canada) by converting samples

https://doi.org/10.5194/egusphere-2025-5020
Preprint. Discussion started: 16 October 2025

to CO_2, then analyzing them in dual-inlet mode on a Thermo Scientific DELTA V Plus IRMS. Approximately 600 ng Sr was extracted and purified via Sr Spec ion chromatography column chemistry in a PicoTrace Laboratory at the Woods Hole Oceanographic Institution (WHOI; USA) and a Thermo Fisher Neptune Multicollector-ICP-MS in the WHOI Plasma Facility was then used to quantify $^{87}Sr/^{86}Sr$ after correcting for Rb interferences and instrumental mass bias (Voss et al., 2014). Analytical blanks were insignificant. Isotope values were normalized to standard reference material NBS 987 $^{87}Sr/^{86}Sr$ = 0.710240. $\Delta^{14}C$-DIC samples were submitted to the André E. Lalonde Accelerator Mass Spectrometry (AMS) Laboratory (University of Ottawa, Canada) where they were purified into CO_2, then analyzed on a 3 MV tandem AMS (Murseli et al., 2019). Method analysis of stable- and radio-organic carbon isotopes ($\delta^{13}C$-DOC, $\delta^{13}C$-POC, $\Delta^{14}C$-DOC, $\Delta^{14}C$-POC) are described in detail in Drapeau et al., 2025b.

Mineralology

X-Ray Diffraction (XRD) was conducted on suspended river sediment collected at our sampling sites on PES filters by the X-Ray Diffraction Laboratory (University of Alberta) to determine minerology phases.

2.3.3 Data analyses

Bicarbonate (HCO_3^-) was calculated via the charge balance of major cation (Ca^{2+}, K^+, Mg^{2+}, Na^+) and anions (Cl^-, SO_4^{2-}) (in mEq L^{-1}) (Schlesinger & Bernhardt, 2013). Minor anions like organic acids and halogens other than Cl^- were assumed to be negligible in our study system and were thus ignored in the calculation (e.g., Hodson et al., 2000). Charge balance-derived HCO_3^- was then checked by interpreting its linear relationship with Ca^{2+} ($R^2_{adj} = 0.84$, $p < 0.001$).

For five sampling events during the first field collection trip (May 2019), major cation data was missing. To include these datapoints in our inversion and inorganic-organic carbon mass balance models, we interpolated the missing chemistry using strong linear relationships ($R^2_{adj} > 0.45$). Ca^{2+}, Mg^{2+}, and Na^+ were interpolated from DIC, while K^+ was interpolated from Si (**Figure S3**). In total, interpolation occurred in five out of 155 sampling events (or, ~3% of cases), but this

https://doi.org/10.5194/egusphere-2025-5020
Preprint. Discussion started: 16 October 2025

inclusion was important due to the general lack of weathering data for spring in glacierized regions globally.

Concentration data that fell below analytical detection limits (DL) were modified to half DL values for statistical purposes (Antweiler & Taylor, 2008; Helsel, 1990). Further, all data from four sampling dates at site AR1 were eliminated from statistical analyses when inputs from an upriver tributary disproportionately influenced the biogeochemical signal (see starred circles in **Figure S2**). Unless otherwise stated, statistics were performed in base R and data figures were built using *ggplot2* (R Core Team, 2022; Wickham, 2016).

Instantaneous CO_2 flux estimations

We calculated instantaneous CO_2 influxes (negative values) to, and effluxes (positive values) from, our study rivers, which provide a more accurate quantification of net CO_2 exchange across the air-water interface than $CO_{2(aq)}$ percent saturation. Instantaneous fluxes were calculated from our measured atmospheric and $CO_{2(aq)}$ concentrations, calculated energy dissipation rates (eD) and modeled gas exchange velocities (k_{600}) (Raymond et al., 2012). k_{600} is the rate that a gas approaches equilibrium at the air-water interface, normalized to a Schmidt number of 600 (Bade, 2009). In this study, the substantial efforts that went into measuring k_{600} in situ were unsuccessful. For example, gross primary productivity (GPP) was low across all sampling sites, preventing us from using dissolved O_2 concentration time series to estimate k_{600} (Hall & Ulseth, 2020); sampling sites with few white rapids and moderately sized waterfalls (i.e., SR3 and AR1) were explored for changes in k_{600} across river discontinuities (Hall & Ulseth, 2020) but all efforts failed, either due to a non-effect on k_{600} or sampling inaccessibility; and while working in Canadian National Parks afforded us relatively pristine sampling conditions, the addition of tracer gases to measure gas exchange velocities was not possible. Given the riverscapes of our three watersheds, and the desire to be methodologically consistent across all sampling sites and times, empirical equations and models were instead used to estimate k_{600} (Hall & Ulseth, 2020).

First, energy dissipation rate (eD), a quantification of turbulence (Ulseth et al., 2019), was calculated. eD relies on gravitational acceleration (9.81 m s^{-2}) and two unknowns, river slope

https://doi.org/10.5194/egusphere-2025-5020
Preprint. Discussion started: 16 October 2025

(unitless) and water velocity (V; m s^{-1}). Slope was appraised using the Alberta Provincial DEM which was downloaded and used in ArcGIS (Alberta Environment and Parks, 2017; ESRI, 2023). Due to the 25 m resolution of the Alberta Provincial DEM, if a sampling site had a steeper slope, we were able to measure its slope within a smaller distance (e.g., within 250 m of site), but if the sampling site slope was gentle, we sometimes had to quantify longer river sections (e.g., within 4000 m of the site). A power relationship was applied to discharge (Q) to determine V for each of our sampling sites and times (**Figure S4**). This power relationship was derived using Q and V measured at four WSC hydrometric gauging stations (**Table S3**) along our rivers from 2019 to 2021 (**Figure S4**). A power relationship was determined for the 56 Q and V point samples (**Eq. 5**; $R^2 = 0.72$); this relationship was then applied to the Q for all sampling sites and times to estimate V:

$$V = 0.30Q^{0.35} \quad \textbf{(Eq.5)}$$

Once eD (m^2 s^{-3}) was calculated, k_{600} was determined by the mountain stream models defined in Ulseth et al., 2019:

$$\text{eD} = \text{gSV} \quad \textbf{(Eq.6)}$$

When eD <0.02, then: $$\ln[k_{600}] = 3.10 + 0.35\ x \ln[eD] \quad \textbf{(Eq.7)}$$

When eD >0.02, then: $$\ln[k_{600}] = 6.43 + 1.18\ x \ln[eD] \quad \textbf{(Eq.8)}$$

To convert k_{600} to the exchange velocity of a particular gas (in our case, k_{CO_2}), Schmidt scaling (Sc_{CO_2}) was applied (**Eq.9**, from Wanninkhof, 2014) and k_{CO_2} was calculated:

$$Sc_{CO_2} = 1923.6 - 125.06\ x\ T_{water} + 4.3773\ x\ T^2{}_{water} - 0.85681\ x\ T^3{}_{water} + 0.00070284\ x\ T^4{}_{water} \quad \textbf{(Eq.9)}$$

$$k_{CO_2} = \frac{k_{600}}{\left(\frac{600}{Sc_{CO_2}}\right)^{-0.5}} \quad \textbf{(Eq.10)}$$

Finally, instantaneous flux (F; g CO_2 m^{-2} d^{-1}) across the air-water boundary was determined (Bade, 2009; Raymond et al., 2012; Wanninkhof, 2014) as:

https://doi.org/10.5194/egusphere-2025-5020
Preprint. Discussion started: 16 October 2025

$$F = k_{CO_2}(CO_{2(water)} - CO_{2(air)}) \quad \textbf{(Eq.11)}$$

Therefore, instantaneous CO_2 fluxes at our sites during all sampling times (except winter) were estimated using the modeled slope and calculations outlined by various foundational contributions.

Inversion model

To partition the dissolved riverine species among various geochemical sources, our study employed the MEANDIR inversion model (Kemeny & Torres, 2021). MEANDIR is well-suited for this work due to its flexibility in selecting major elements and incorporating isotopic tracers (e.g. $\delta^{34}S$). The model solves an over-determined system of equations to quantify endmember contributions (fractions, f_i) to observed solute concentrations for X = Ca^{2+}, Mg^{2+}, Na^+, Cl^-, SO_4^{2-} as follows:

$$\left(\frac{X}{\Sigma^{\pm}}\right)_{river} = \sum_{i=1}^{n} f_i \left(\frac{X}{\Sigma^{\pm}}\right)_i \quad \textbf{(Eq.12)}$$

$$\left(\frac{^{34}S}{^{32}S} \cdot \frac{SO_4^{2-}}{\Sigma^{\pm}}\right)_{river} = \sum_{i=1}^{n} f_i \left(\frac{^{34}S}{^{32}S} \cdot \frac{SO_4^{2-}}{\Sigma^{\pm}}\right)_i \quad \textbf{(Eq.13)}$$

$$\sum_{i=1}^{n} f_i = 1 \quad \textbf{(Eq.14)}$$

Here $\Sigma^{\pm}$ is the sum of concentrations of Ca^{2+}, Mg^{2+}, Na^+ and SO_4^{2-} in μM used for normalization. i represents endmembers (n = 5), which includes precipitation, evaporite weathering, carbonate weathering, silicate weathering, and pyrite. $\left(\frac{X}{\Sigma^{\pm}}\right)_{river}$ are the concentration ratios of each river sample, while $\left(\frac{X}{\Sigma^{\pm}}\right)_i$ and $\left(\frac{^{34}S}{^{32}S} \cdot \frac{SO_4^{2-}}{\Sigma^{\pm}}\right)_i$ are ratios for the ith endmember as the input of MEANDIR. The elemental and isotopic ratios for the five endmembers were sourced from the global compilation by Burke et al. (2018), which provides representative ranges for major geologic

https://doi.org/10.5194/egusphere-2025-5020
Preprint. Discussion started: 16 October 2025

terranes (**Table 1**). This global dataset was deemed suitable for our study region, which is characterized by a mix of sedimentary carbonate and silicate lithologies.

To simplify calculations and reduce dependence on reference frames, $\delta^{34}S$ was converted to $\frac{^{34}S}{^{32}S}$ ratios (Kemeny & Torres, 2021). This conversion removed reliance on the arbitrary 0 ‰ standard, ensuring consistency in the analysis. While data for elements like K^+, Si, and HCO_3^- were available, they were excluded from the endmember mixing analysis due to their non-conservative behavior caused by biological activity (Carey & Fulweiler, 2013; Talling, 2010) or atmosphere-water exchange (Raymond et al., 2013).

For each river sample, a Monte Carlo approach was employed to generate up to 10^6 endmember ratios $\left(\frac{X}{\Sigma^{\pm}}\right)_i$, assuming a uniform distribution within the defined ranges. The process terminates early if 25 qualified groups of endmember ratios are identified, where qualified groups are defined as those with: (1) $0 \leq f_i \leq 1$, (2) normalized major element ratios within 15 % error from the river sample ratios, and (3) $\delta^{34}S$ values within 1 ‰ of the measured value. For each iteration, the over-determined system of equations 8-10 is solved by optimizing a cost function that minimizes the proportional misfit of inversion, with equal weighting on all variables. The median values of f_i from the 25 qualified groups were utilized for analysis, while the corresponding 25th and 75th percentiles represent uncertainties. Out of 155 samples, 153 were successfully inverted. The two failed samples (i.e., SR1 and NSR1 in autumn 2020) were excluded due to anomalously high $\left(\frac{Ca}{\Sigma^{\pm}}\right)_{river}$ ratios and low $\left(\frac{Na}{\Sigma^{\pm}}\right)_{river}$ ratios.

Table 1. Endmember ratios used in MEANDIR sourced from Burke et al. (2018).

Parameter	Carbonate	Silicate	Evaporite	Precipitation	Pyrite
Ca^{2+}	0.317-1.000	0.039-0.591	0.012-0.660	0.005-0.061	0.000-0.000
Mg^{2+}	0.000-0.675	0.000-0.466	0.000-0.159	0.133-0.185	0.000-0.000
Na^+	0.000-0.013	0.209-0.677	0.128-0.520	0.685-0.757	0.000-0.000
Cl^-	0.000-0.000	0.000-0.000	0.078-0.562	0.680-0.980	0.000-0.000
SO_4^{2-}	0.000-0.000	0.000-0.000	0.031-0.479	0.061-0.113	1.000-1.000
$\delta^{34}S\text{-}SO_4$	10.00-30.00	0.000-5.000	10.00-30.00	15.00-20.00	-40.00-40.00

Note. All ratios are normalized to the sum of the observations and are uniform in distribution.

https://doi.org/10.5194/egusphere-2025-5020
Preprint. Discussion started: 16 October 2025

Estimation of TDS proportions

We determined the proportion of relative total dissolved solids (TDS) from precipitation, atmosphere, evaporite, carbonate, silicate, and pyrite endmembers to quantify the mass of material being exported downriver from each sampling site. Median proportions Ca^{2+}, Mg^{2+}, Na^{+}, Cl^{-}, and SO_4^{2-} for each endmember were determined by MEANDIR as described above, whereas ion species that were not included in the inversion model required estimation. K^{+} derived from silicate weathering was set at $K^{+}/Na^{+} = 0.1$ (Gaillardet et al., 1999), with other geologic sources producing none (assuming sylvite, or KCl, is rare in the study area), and that from precipitation calculated as (K^{+}_{river} - $K^{+}_{silicate}$). HCO_3^{-} contributions from weathering were estimated based on reaction stoichiometry. For carbonate weathering by carbonic acid (e.g., **Eq. 1** above), one mole of HCO_3^{-} is derived from rock and one from the atmosphere. Therefore, the atmospheric contribution to TDS was estimated as half the molar sum of carbonate-derived Ca^{2+} and Mg^{2+}. For silicate weathering (e.g., **Eq. 3** above), both moles of HCO_3^{-} are derived from the atmosphere, so the full molar sum of silicate-derived cations was attributed to the atmospheric component. HCO_3^{-} was set as zero for pyrite, and evaporites; not estimated for organic processes; and was calculated as ($HCO_3^{-}{}_{river}$ - $HCO_3^{-}{}_{carbonate}$ - $HCO_3^{-}{}_{silicate}$) for precipitation. Lastly, all measured dissolved silica was attributed to the silicate weathering endmember ($SiO_{2silicate} = SiO_{2river}$).

Inorganic-organic carbon mass balance model

We diverged from weathering mass balance models traditionally used in proglacial freshwaters (e.g., Deuerling et al., 2019; Hodson et al., 2000; St. Pierre et al., 2019) because they exclusively focus on inorganic biogeochemical constituents. Instead, we took an integrative approach using models that included both inorganic and organic constituents due to an assumed increase in both autochthonous and allochthonous organic matter inputs with increasing distance downriver from source glaciers (S. P. Anderson, 2007; Robison et al., 2023). To determine the fraction of riverine DIC sourced from carbonate weathering and atmospheric $CO_{2(g)}$, silicate weathering, and the respiration of OC, we used a combination of multiple mass balances to estimate an overall inorganic-organic carbon mass balance, as detailed in Voss et al., (2023), which included concentrations of dissolved ions (Ca^{2+}, Mg^{2+}, Na^{+}, SO_4^{2-}, Cl^{-}), DIC, and DOC, as well as the stable

https://doi.org/10.5194/egusphere-2025-5020
Preprint. Discussion started: 16 October 2025

carbon isotope composition of DIC and DOC. As ^{13}C-DOC samples were not collected at all sampling sites and times (Drapeau et al., 2025b), only 86 of 155 samples were included in the mass balance.

The calculations included in the inorganic-organic carbon mass balance can be found in the Supplementary Information (**Text S1**) and in Voss et al., (2023). Briefly, the steps of the mass balance were as follows: (1) The dissolved ions and DIC were sea salt corrected (ion_{nss}) using Cl^- as published in Gaillardet et al., 1999. (2) The fraction of riverine DIC sourced from carbonate weathering and non-carbonate weathering were determined using known measured and carbonate endmember ions and DIC. (3) The fraction of sulfuric acid (H_2SO_4) and carbonic acid (H_2CO_3) involved in weathering reactions was apportioned. (4) The fraction of $\delta^{13}C$ sourced from carbonate weathering, non-carbonate weathering, and OC respiration was determined. (5) The fraction of DIC sourced from silicate weathering and OC respiration, and the atmosphere was calculated. (6) The fraction of DIC from silicates alone was isolated using carbonate and silicate $Ca^{2+}_{nss}/Na^{+}_{nss}$ endmembers. This fraction was used to determine the concentration of Na^+ and HCO_3^- that were derived from silicates and non-silicates. (7) Lastly, the concentration of DIC from carbonate weathering, silicate weathering, and OC respiration was determined and converted into percentages for data analysis. Carbonate and silicate end members (carbEM and silEM, respectively) for these calculations can be found in **Table 2**.

As explored in Voss et al., (2023), this mass balance assumes that DIC is derived and/or influenced by carbonate or silicate weathering, OC respiration, and atmospheric CO_2 influx, ignoring the loss of DIC from riverine CO_2 efflux, in-river DOC mineralization or biological consumption, and carbonate mineral precipitation. We also acknowledge that in applying a mass balance model developed for downriver freshwater systems on the western side of the Canadian Cordillera (Fraser River) that uses some endmembers from the literature rather than site-specific endmembers, we potentially overestimate the role of organics in defining the biogeochemistry of our most upriver sites (i.e., SR1, SR2, NSR1, and BR1). However, we consider an overestimation of the influence of DOC in our study system as less egregious than overestimating the combined influence of carbonate and silicate weathering, which is the focus of this study. Consequently, calculated weathering outputs are likely conservative.

https://doi.org/10.5194/egusphere-2025-5020
Preprint. Discussion started: 16 October 2025

Table 2. Endmember values used in the inorganic-organic carbon mass balance

Parameter	$Ca^{2+}_{nss}/Na^{+}_{nss}$*	$HCO_3^-{}_{nss}/Na^{+}_{nss}$**	$\delta^{13}C$***
Carbonate endmember (carbEM)	326	120	-8.25
Silicate endmember (silEM)	16	2	0.5

Note. *From this study. **From Gaillardet et al., 1999. ***From Spence & Telmer, 2005

3 Results & discussion

3.1 Quantifying dissolved CO_2 variability

3.1.1 $CO_{2(aq)}$ is undersaturated immediately downriver of glaciers

Measurements revealed that $CO_{2(aq)}$ was highly undersaturated at some sampling sites along our study rivers, especially those nearest source glaciers. Mean ± SD $CO_{2(aq)}$ percent saturation was 106 ± 34%, with the minimum value recorded in spring at SR1 (16%) and the maximum value recorded in early spring at BR2 (222%). Regardless of season, SR1, the site closest to a source glacier, consistently had the lowest $CO_{2(aq)}$ percent saturation, whereas BR2, a wetland site (**Figure 2, Table S2**) (Serbu, St. Louis, et al., 2024), consistently had the highest $CO_{2(aq)}$ percent saturation (**Figure 3**). The Sunwapta-Athabasca River and North Saskatchewan River exhibited similar patterns in $CO_{2(aq)}$ percent saturation with the upriver sites being the most undersaturated before increasing to, or above, saturation at their respective glacial outwash plain sites (i.e., SR3, NSR2) (**Figure 3A**). This pattern diverged along the BR, as all sites were oversaturated in $CO_{2(aq)}$ at all sampling times (**Figure 3A**). Notably, BR1 is immediately downriver of a waterfall discontinuity (Hall & Ulseth, 2020). The river-atmosphere equilibration at this discontinuity may have then masked any in situ gaseous signatures of weathering. Seasonal variability was also observed in $CO_{2(aq)}$ percent saturation (**Figure 3A**). $CO_{2(aq)}$ percent saturation generally decreased from spring through summer before increasing in autumn and remaining elevated until the following spring (**Figure 3A**; **Table S4**). Undersaturation was captured at all times of year except winter (**Table S4**), when groundwater feeds the hydrologic system, even immediately downriver of glacial influence in our study region (Hayashi, 2020; Paznekas & Hayashi, 2016). Seasonal trends in $CO_{2(aq)}$ percent undersaturation were especially prominent at SR1, SR2, and NSR1.

https://doi.org/10.5194/egusphere-2025-5020
Preprint. Discussion started: 16 October 2025

3.1.2 Net CO_2 consumption occurs near glaciers

Instantaneous CO_2 fluxes ranged from -149 to 56 g CO_2 m^{-2} d^{-1} across the open water season (May 1 to October 31), where negative values relate to influxes from the atmosphere to the river and positive values relate to effluxes from the river to the atmosphere. For context, fluxes from mean global compilations of tropical forest and wetlands are -12.6 and -12.3 g CO_2 m^{-2} d^{-1}, respectively, and those from boreal forest and tundra are -1.3 and -0.9 g CO_2 m^{-2} d^{-1}, respectively (IPCC, 2001). This means that our most negative flux was nearly 12 times more CO_2 consumptive than tropical forests and a whopping 166 times more CO_2 consumptive than the tundra. Instantaneous fluxes were generally most negative at SR1 and NSR1, sites closest to source glaciers (**Figure 3B**), indicating CO_2 influx to the river from the atmosphere. Fluxes quickly leveled out at or near zero (neutral) at sites immediately downriver, for example at SR2 (**Figure 3B**). The SR2 site was the outflow of the Sunwapta proglacial lake, a known sediment trap (Wankiewicz, 1979); the rapid change in flux between SR1 and SR2 could indicate the potential loss of easily weatherable material that initially emerged from the Columbia Icefield subglacial environment (Mancini et al., 2023). By comparison, the Saskatchewan Glacier was the largest of the source glaciers in this study. Theoretically, with more glacier area in direct contact with underlying bedrock, more sediment-laden meltwaters could be expelled from the system. The NSR1 site was approximately 5.6 km downriver of its glacial tongue and downriver of the Saskatchewan proglacial lake (Serbu et al. 2024), yet we generally saw greater negative instantaneous CO_2 fluxes at this site than others in the study (**Figure 3B**). None of the sites along the Bow River had negative instantaneous CO_2 fluxes, and similar to CO_2 saturation, several Bow River sites had some of the highest positive fluxes in this study (**Figure 3B**). For example, the wetland site BR2 produced the highest instantaneous CO_2 fluxes in spring while BR1 had the highest in autumn (**Figure 3B**).

Instantaneous CO_2 fluxes also showed distinct seasonality. Fluxes from all sites were closest to net equilibrium in spring and autumn, and most negative during summer (**Table S4**). This seasonal effect was most prominent at SR1 and NSR1, where CO_2 influx into the rivers was greatest in summer (**Figure 3B**). Fluxes at AR2 remained close to neutral across all seasons except during summer 2020, where they increased to the highest positive instantaneous flux calculated in this study (**Figure 3B**). Site AR2 is likely affected by in situ biological productivity because it is

https://doi.org/10.5194/egusphere-2025-5020
Preprint. Discussion started: 16 October 2025

receiving more allochthonous terrestrial organic matter (Robison et al., 2023) than upriver sites along the Sunwapta-Athabasca River, leading to the observed net efflux of CO_2 from the river. The same seasonal trend, though muted compared to AR2, is observed at other downriver sampling sites such as SR3 and BR4 (**Figure 3B**), indicating that the majority of our downriver sampling sites behave similarly to other mountain rivers, acting as net sources of CO_2 to the atmosphere (Horgby et al., 2019).

https://doi.org/10.5194/egusphere-2025-5020
Preprint. Discussion started: 16 October 2025

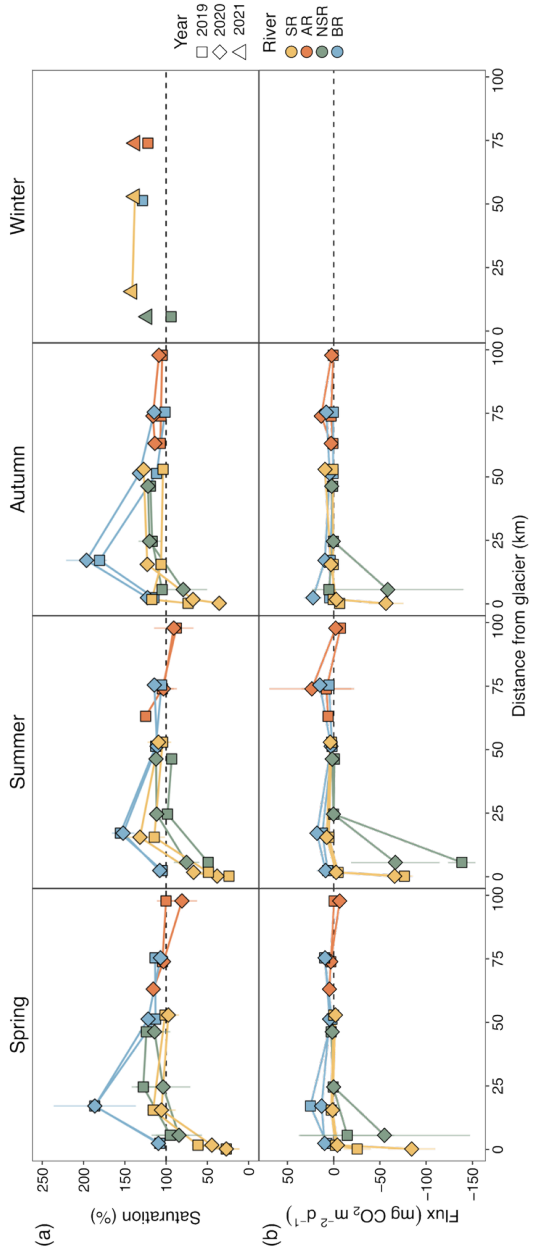

Figure 3. (A) CO_2 percent saturation and (B) modeled instantaneous CO_2 fluxes for riverine sampling sites at increasing downriver distance from source glaciers across the open water seasons in 2019 and 2020. Dashed lines represent (A) saturation, and (B) a net flux of zero, where above zero CO_2 is fluxing out of the rivers and below zero CO_2 is fluxing into the rivers. Seasons are binned by sampling dates and are summarized in **Table S4**. Rivers are abbreviated as SR (Sunwapta River), AR (Athabasca River), NSR (North Saskatchewan River), and BR (Bow River).

https://doi.org/10.5194/egusphere-2025-5020
Preprint. Discussion started: 16 October 2025

3.2 A first glance at weathering trends in geochemistry and minerology

3.2.1 Ion chemistry and mineralogy are uniform between sampling sites

Piper diagrams indicate that all our sampling sites contained similar ratios of dissolved cations and anions (**Figure 4**), and that calcium bicarbonate dominated the ion pool. This is indicative of similar lithologies across all sampling sites, which was supported in part by local geologic maps (Pana & Elgr, 2013; **Figure 1**) and the general consistency across sites in our XRD results (**Figure S5**). We acknowledge that the XRD data presented here is a non-encompassing, qualitative (i.e., present/absent) measure based on the characteristic peaks of each mineral (Bish & Plötze, 2010). XRD data is also typically imperfect as particular mineral phases can undergo geochemical reactions that result in their absence during analysis. For instance, pyrite undergoes rapid oxidative weathering when in contact with the atmosphere (J. E. Johnson et al., 2014). Regardless, the XRD data collected across our sampling sites suggests regional minerology was largely driven by carbonate and silicate minerals, including albite, calcite, clinochlore, chlorite-serpentine, dolomite, muscovite, quartz, and rutile (**Figure S5**).

https://doi.org/10.5194/egusphere-2025-5020
Preprint. Discussion started: 16 October 2025

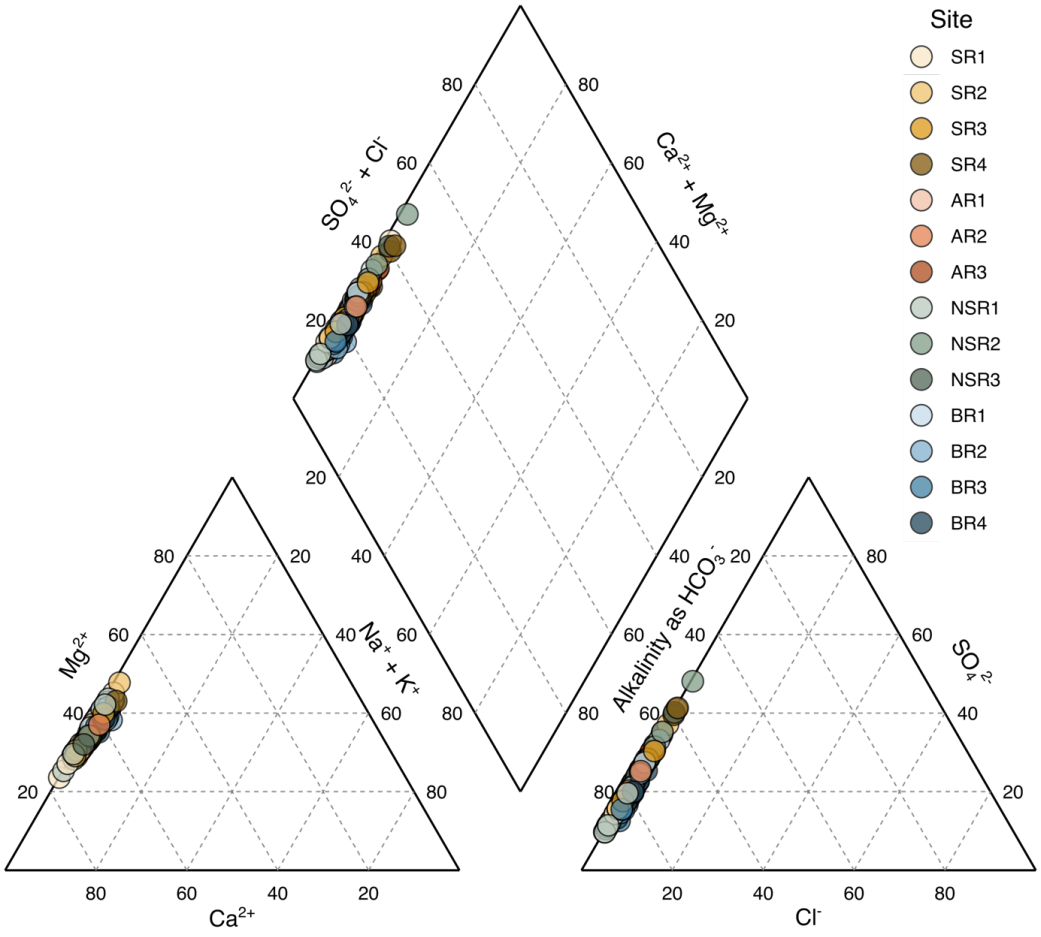

Figure 4. Piper diagram of all major cation and anion concentrations (in mEq L^{-1}) along our study rivers, color-coded by sampling site. Rivers are abbreviated as SR (Sunwapta River), AR (Athabasca River), NSR (North Saskatchewan River), and BR (Bow River).

3.2.2 Isotope compositions are primarily dependent on river and distance from glacier, not season

$^{87}Sr/^{86}Sr$ values aligning with the lowest and highest $Ca^{2+}_{nss}/Na^{+}_{nss}$ and $Mg^{2+}_{nss}/Na^{+}_{nss}$ molar ratios within each of the four rivers were quantified (n=8; **Figure S6**). To aid in the interpretation of our results, matching $^{87}Sr/^{86}Sr$ and chemistry data from Arendt et al. (2016) collected proximal to SR1 across the 2011 glacier melt season were also assessed. At SR1, which is fed directly by Athabasca

https://doi.org/10.5194/egusphere-2025-5020
Preprint. Discussion started: 16 October 2025

Glacier meltwaters, Arendt et al. (2016) determined that weathering products were dominated by silicate-derived solutes during initial glacial melt in May, but that carbonate-derived weathering products dominated during peak flow in July. A presence of subglacial weathering has been shown to produce dissolved $^{87}Sr/^{86}Sr$ values in meltwaters that are more radiogenic than that of the original bedrock (Andrews & Jacobson, 2018; Stevenson et al., 2016), yet temporal trends were still clear (Arendt et al., 2016). By contrast, the samples analyzed for $^{87}Sr/^{86}Sr$ in this study were from a wide area. $^{87}Sr/^{86}Sr$ values ranged from 0.7099 to 0.7199 (**Figure S7**), with a mean of 0.7126, i.e., slightly more radiogenic than global river export to the ocean (0.71106; Peucker-Ehrenbrink & Fiske, 2019). Sites along the Sunwapta and Athabasca rivers exhibited trends in 1/Sr, Ca/Mg, Ca/K, and $^{87}Sr/^{86}Sr$ that suggested relatively more upriver carbonate-derived and downriver silicate-derived weathering products (Arendt et al., 2016); the same pattern did not emerge along the North Saskatchewan or Bow rivers (**Figure S7**). Of particular interest was sampling site AR3, which had the most radiogenic $^{87}Sr/^{86}Sr$ despite Sr concentrations similar to other sites. A possible explanation is that this downriver sampling site better captured the $^{87}Sr/^{86}Sr$ signature of weathered K-rich mica such as muscovite, which was present along our study rivers (**Figure S5**), than at upriver sites due to the increased size of the watershed area (S. P. Anderson et al., 1997; Hindshaw et al., 2014). This potential explanation aligns with the fact that K-rich mica (e.g., biotite) is preferentially weathered in glacierized watersheds (Blum & Erel, 1995; Dixon & Thorn, 2005).

The $\delta^{34}S$-SO_4 (VCDT) and $\delta^{18}O$-SO_4 (‰ VSMOW) of our rivers ranged from 8 to 29 ‰ and -17 to 4‰, respectively, with a small yet distinct grouping of values between rivers. The most isotopically light $\delta^{34}S$-SO_4 values were measured in the Sunwapta River, followed by the Athabasca, Bow, and North Saskatchewan Rivers, which had the most isotopically heavy $\delta^{34}S$-SO_4 values overall (**Figure 5A**). There were no notable trends when assessed by season (**Figure 5B**). The $\delta^{34}S$-SO_4 values measured in this study were similar to global evaporites (10-30 ‰) (**Figure 5C**), with our mean value of 17 ‰ aligning with the global evaporite mean of 17 ‰ (Burke et al., 2018). However, microbial sulfate reduction and lithogenic sulfides encompass a wide span of $\delta^{34}S$-SO_4 values (Burke et al., 2018; Kemeny et al., 2021; Relph et al., 2021), making it difficult to apportion data to these processes. For context, the $\delta^{34}S$ of pyrite measured from the Burgess Shale and Stephen Formations on the western slopes of the Canadian Rocky Mountains broadly

https://doi.org/10.5194/egusphere-2025-5020
Preprint. Discussion started: 16 October 2025

ranges from -2 to nearly 30 ‰ (Gaines et al., 2012), overlapping greatly with our river data (**Figure 5D**). These data are thus inconclusive on their own.

https://doi.org/10.5194/egusphere-2025-5020
Preprint. Discussion started: 16 October 2025

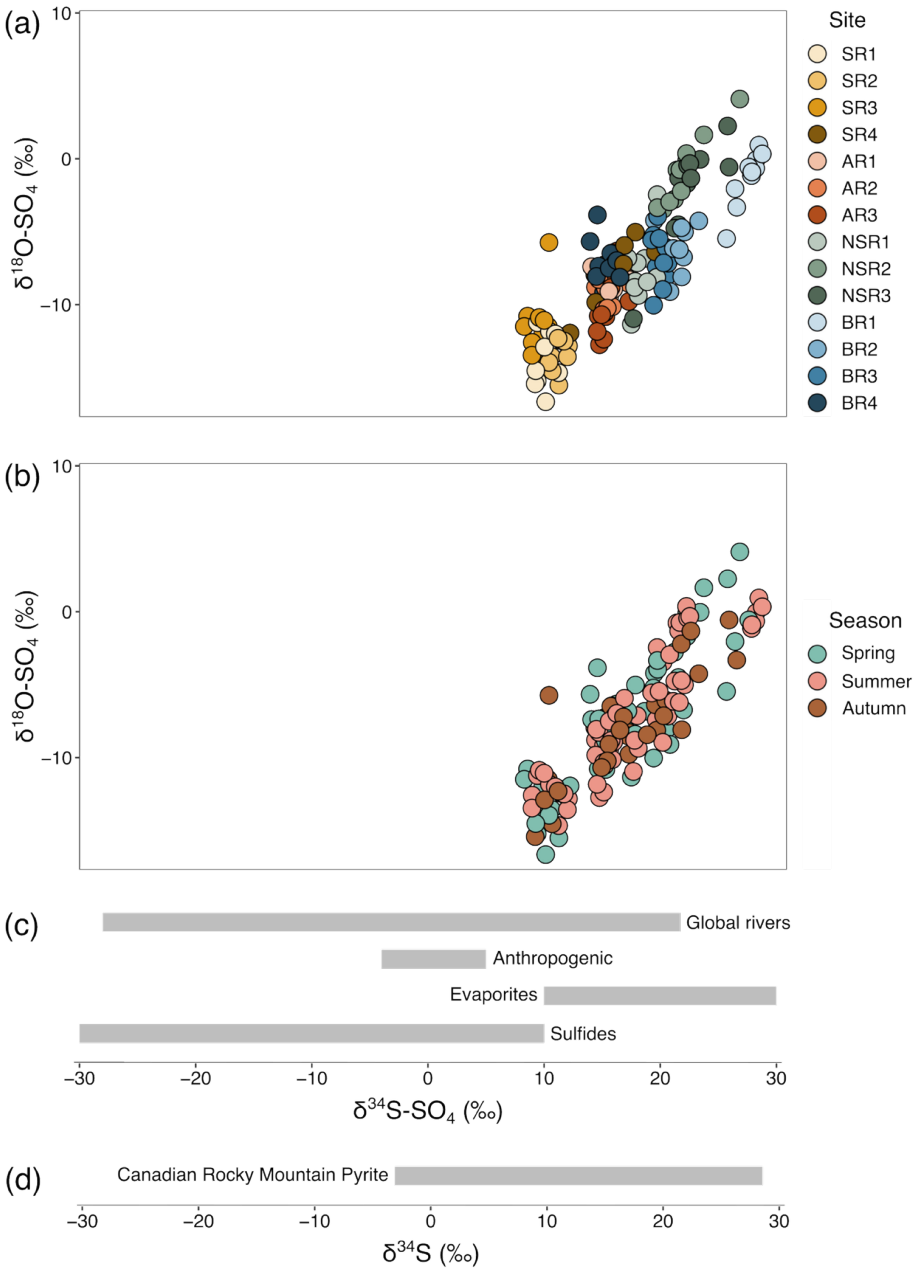

Figure 5. $\delta^{34}S\text{-}SO_4$ (‰ VCDT) versus $\delta^{18}O\text{-}SO_4$ (‰ VSMOW) for sampling sites (A) along the Sunwapta (SR), Athabasca (AR), North Saskatchewan (NSR), and Bow (BR) rivers, and (B) across seasons. (C) The global river, anthropogenic, evaporite, and sulfide range of $\delta^{34}S\text{-}SO_4$ is adapted from Burke et al. (2018). (D) A range of $\delta^{34}S$ for Canadian Rocky Mountain pyrite is from Gaines et al., (2012). Figure adapted from Relph et al. (2021).

https://doi.org/10.5194/egusphere-2025-5020
Preprint. Discussion started: 16 October 2025

δ^{13}C-PIC ranged from -3.18 to 0.55 ‰ with no discernable downriver trends (**Figure S8**). The small spread of δ^{13}C-PIC (**Figure S8**) aligned with the isotope value of eroded carbonates, consistent with other alpine locales such as the Rhône River system (Aucour et al. 1999). Matching δ^{13}C-DIC had an overall larger range from -7.32 to -2.08 ‰ (**Figure S8**) and were isotopically heaviest at sampling sites closest to the source glacier, suggesting relatively more carbonate contributions to the DIC pool at these sites (**Figure S8**, **Figure 6A**) (Marwick et al., 2015). Downriver sites were generally isotopically lighter, potentially indicating contributions from organic sources to the DIC pool (Marwick et al., 2015), or greater contributions from silicate weathering, which would have a DIC value reflective of a mixture of soil carbon and atmospheric CO_2 (**Figure 6A**). An equal contribution of carbonates and C3 plants, which dominate vegetated landscapes of the Canadian Rocky Mountains, would have an approximate isotopic value of -10 ‰ (Aucour et al., 1999). Yet, even with the downriver isotopic shift, δ^{13}C-DIC values never fell below -8 ‰ along any river (**Figure S8**, **Figure 6A**), suggesting an overall larger contribution of carbonate sources to the DIC pool at all sites. Although periphyton (benthic algae) in our study rivers (Bowman et al., 2005, 2007) may contribute to the downriver shift in δ^{13}C-DIC (**Figure 6A**), the isotope values of periphyton are difficult to constrain (Ishikawa et al., 2012), and therefore a detailed discussion is beyond the scope of this study.

Δ^{14}C-DIC spanned from -644 to -205 ‰, though samples were only collected from the first two sites on the Sunwapta, North Saskatchewan, and Bow rivers (except for an individual datapoint at AR1). Downriver sites typically also had Δ^{14}C-DIC indicative of more modern sources than sampling sites closer to the source glacier (**Figure 6A**). SR1 had the lowest Δ^{14}C-DIC values, closest to Δ^{14}C-dead $CaCO_3$ than any other site (**Figure 6A**). All other sites were clustered less negatively and reflect a transition towards a mixture of atmospheric and terrestrial organic contributions to the DIC pool (**Figure 6A**). There were no obvious patterns when δ^{13}C-DIC and Δ^{14}C-DIC were assessed by season (**Figure 6B**).

https://doi.org/10.5194/egusphere-2025-5020
Preprint. Discussion started: 16 October 2025

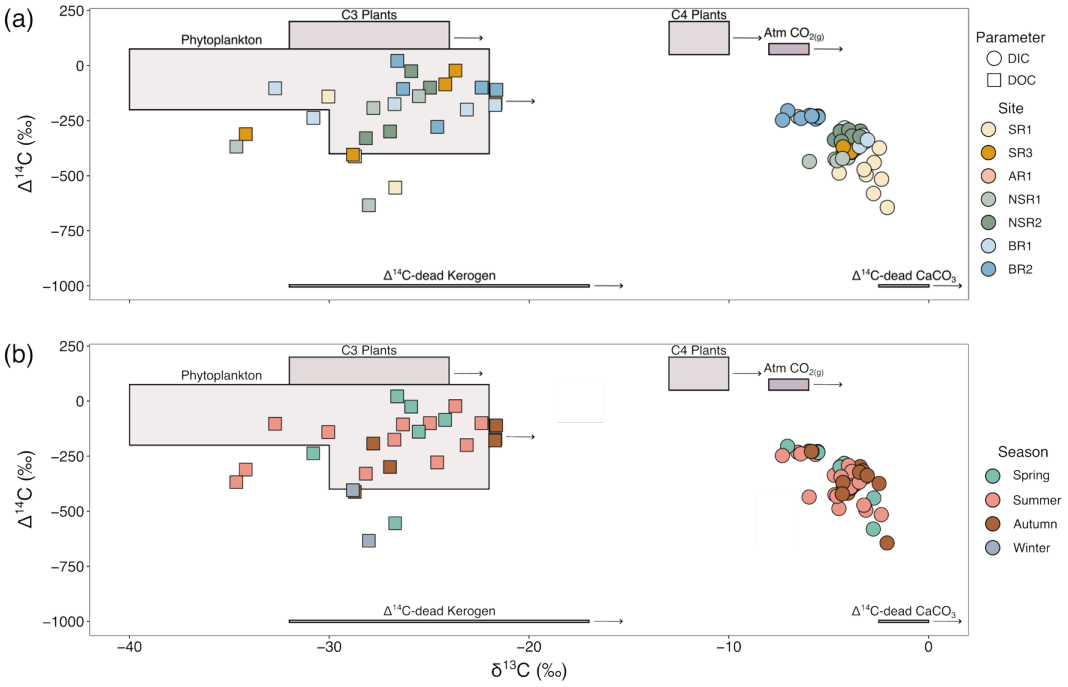

Figure 6. The δ^{13}C (‰) versus Δ^{14}C (‰) of dissolved inorganic carbon (DIC) and dissolved organic carbon (DOC) for sampling sites (A) along the Sunwapta (SR), Athabasca (AR), North Saskatchewan (NSR), and Bow (BR) rivers, and (B) across seasons. Arrows indicate a shift of δ^{13}C (‰) values due to natural fractionations associated with dissolution of carbon in aqueous solutions. DOC data are published in Drapeau et al., (2025a) and Drapeau et al., (2025b). Figure adapted from Voss et al. (2022) and Marwick et al. (2015), with global data from Marwick et al. (2015).

https://doi.org/10.5194/egusphere-2025-5020
Preprint. Discussion started: 16 October 2025

3.3 Inversion modeling confirms ion and acid sources primarily change with distance downriver of the glaciers, not by season

To quantitatively confirm the weathering processes suggested by our elemental and isotopic geochemical data, the MEANDIR inversion model was applied (Kemeny & Torres, 2021). The MEANDIR model was used to partition the observed solute loads into the five defined endmembers (i.e., precipitation, evaporite, carbonate, silicate, and pyrite). **Figure 7** illustrates the median proportional contributions of these endmembers to each major ion at our sampling sites. With all sampling sites and seasons averaged, the median (25th – 75th percentile) proportion of carbonate contributions to Ca^{2+} and Mg^{2+} in our watersheds were 0.93 (0.84 – 1.02) and 0.96 (0.89 – 1.02), respectively (**Table S5**). The dominance of carbonate contributions to these ions is not surprising; even so, slight trends of increased silicate and/or evaporite contributions at downriver sites along each river were apparent (**Figure 7A**). Contributions to Na^{+} were more evenly distributed across all endmembers except pyrite, which does not contribute sodium. Median precipitation, evaporite, carbonate, and silicate proportions for Na^{+} were 0.16 (0.02 – 0.33), 0.20 (0.0009 – 0.37), 0.24 (0.12 – 0.36), and 0.39 (0.28 – 0.51), respectively (**Table S5**). While no sole endmember controlled contributions to Na^{+} across all sampling sites, there was a distinct trend of increasing silicate contributions at downriver sites along each river (**Figure 7A**). The exception to this was the Bow River, whose greatest silicate contributions occurred at the sampling site closest to the glacier. Precipitation, evaporite, carbonate, and silicate contributions to Na^{+} were similar between seasons, with silicate contributing the greatest proportion (**Figure 7B**). Contributions to Cl^{-} were split between precipitation at 0.41 (0.02 – 0.99) and evaporite at 0.59 (0.005 – 0.98) (**Table S5**). The proportion from precipitation was greater at more upriver sites compared to those downriver (**Figure 7A**) and increased from spring to autumn (**Figure 7B**). Greater volumes of glacier and snow melt are captured at river sites in the glacierized portion of the alpine altitudinal life zone (i.e., SR1, SR2, NSR1, BR1) (**Table S2**), driving trends in Cl^{-}. The influence of this direct precipitation input is diluted at more downriver sites due to a relative increase in other water sources, such as groundwater, which could flush evaporite-derived Cl^{-} into the main river stem. The small increase of precipitation contributions throughout the open water season (May – October) is difficult to explain as we might expect higher precipitation-derived Cl^{-} during spring freshet when snowmelt flushes the hydrological system. However, glacier melt intensifies until

https://doi.org/10.5194/egusphere-2025-5020
Preprint. Discussion started: 16 October 2025

peak flow in late summer/early autumn in this alpine region and this, combined with summer and autumn precipitation, could be the reason for the increase. Lastly, 0.98 (0.85 – 0.99) of SO_4^{2-} at all sampling sites was from the pyrite endmember (**Table S5**). Contributions were consistently high moving down each river, with the exception of Bow River which showed an increased, though still small, proportion of evaporite contributions to SO_4^{2-} at downriver sites (**Figure 7A**). The pyrite endmember also dominated contributions to SO_4^{2-} across all seasons (**Figure 7B**).

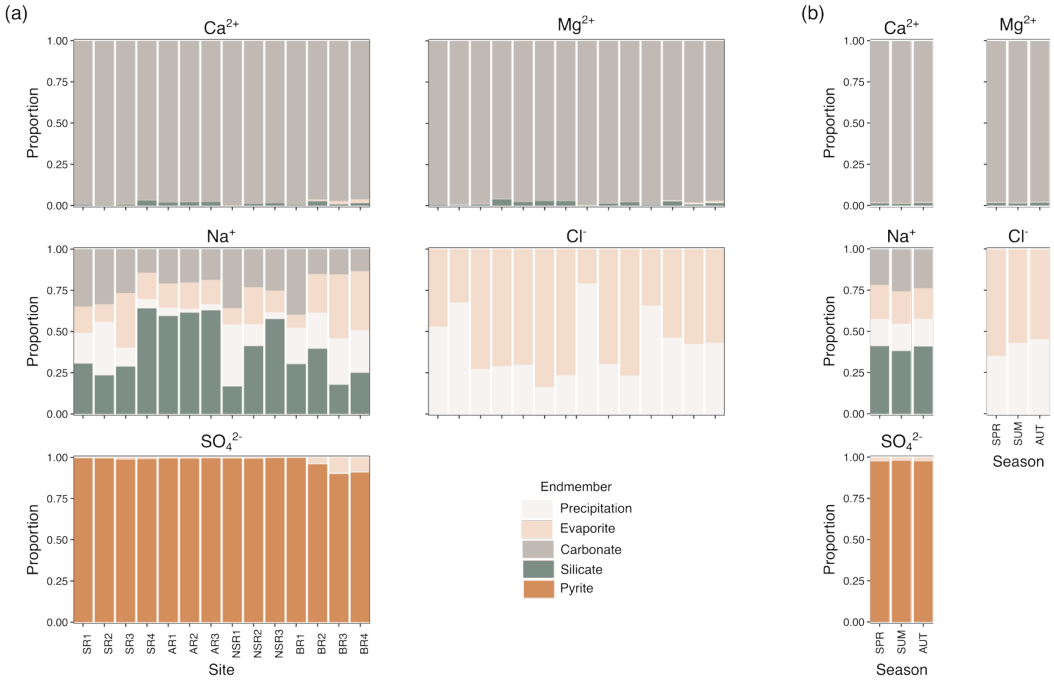

Figure 7. Median proportions of precipitation, evaporites, carbonate, silicate, and pyrite endmembers for dissolved river Ca^{2+}, Mg^{2+}, Na^{+}, Cl^{-}, and SO_4^{2-} for sampling sites (A) along the Sunwapta (SR), Athabasca (AR), North Saskatchewan (NSR), and Bow (BR) rivers, and (B) across seasons. Mean values of each proportion were taken for each sampling site and season.

Expanding on our discussion of ion contributions, we next determined the proportion of relative TDS from the same five endmembers to quantify the mass of material being exported downriver from each sampling site and across seasons. Overall, carbonate-derived weathering products dominated TDS contributions across all sampling sites (proportions ± SD as 56.4 ± 6.8 or greater) and seasons (64.1 ± 12.8) (**Figure 8**, **Table S6**), which is consistent with the limestone and dolomite formations in the region (**Figure S1**) (Gadd, 2009). Silicate-derived weathering products

https://doi.org/10.5194/egusphere-2025-5020
Preprint. Discussion started: 16 October 2025

made up a small proportion of TDS at each sampling site (between 1.48 ± 0.54 at SR1 to 4.01 ± 1.29 at AR3) but generally increased from upriver to downriver sites along the same river (**Figure 8A**, **Table S6A**). Seasonal differences were minimal (between 2.72 ± 0.94 at during summer to 3.51 ± 2.17 during autumn) (**Figure 8B**, **Table S6B**). Low $TDS_{silicate}$ is likely because silicate weathering is depressed in cold environments due to the higher activation energy required to bring the geochemical reaction to completion (S. P. Anderson, 2005) and carbonates weathering preferentially over other geology (Blum et al., 1998). By comparison, pyrite-derived weathering products varied by sampling site (15.9 ± 8.6 at AR2 to 23.7 ± 17.8 at SR3) and season (14.6 ± 2.6 during winter to 26.81 ± 16.2 during autumn) (**Figure 8**, **Table S6**). The differences between sampling sites may have been due to minor differences in local geology, whereas differences between seasons may have been from the influence of water routing. The atmospheric TDS fraction, estimated from half the alkalinity from carbonate weathering plus all the alkalinity from silicate weathering, had the second greatest proportion of relative TDS across all sampling sites (26.7 ± 7.1 at SR1 to 46.1 ± 8.3 at SR3) and seasons (36.6 ± 9.7 during summer to 52.7 ± 9.9 during winter) (**Figure 8**, **Table S6**). The high TDS values from the atmosphere endmember aligns with the expectation of comparatively increased atmospheric deposition at the high elevation sites of this study (Nanus et al., 2003). However, it should be noted that because we ignored organic processes in the HCO_3^- estimation, we likely overestimated both the carbonate and subsequent atmospheric TDS.

https://doi.org/10.5194/egusphere-2025-5020
Preprint. Discussion started: 16 October 2025

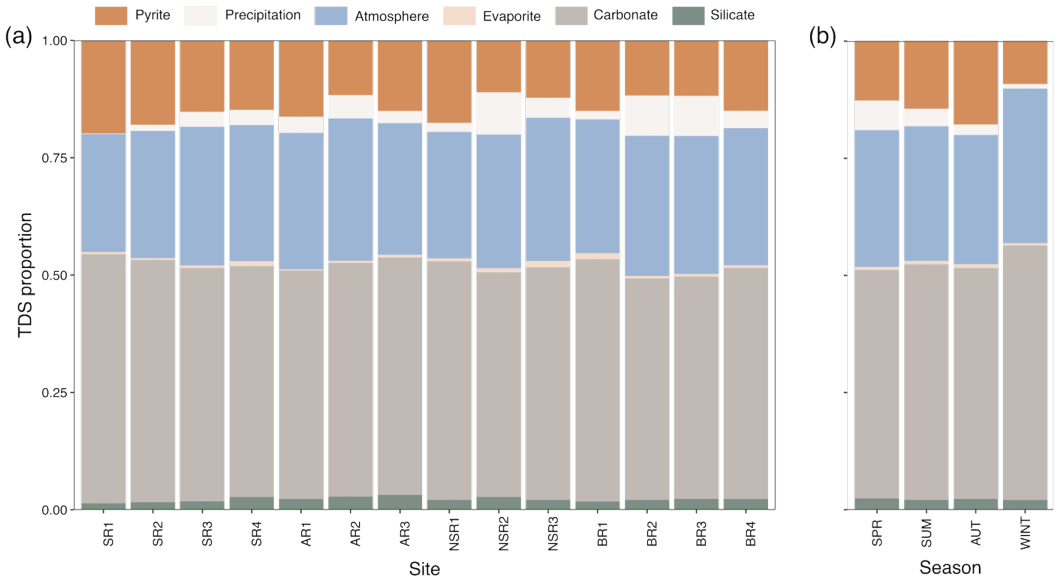

Figure 8. The proportion of relative total dissolved solids (TDS; no units) from precipitation, atmosphere, evaporite, carbonate, silicate, and pyrite endmembers for sampling sites (A) along the Sunwapta (SR), Athabasca (AR), North Saskatchewan (NSR), and Bow (BR) rivers, and (B) across seasons.

The median fraction of weathering cations from carbonate dissolution (R) and median fraction of weathering acid from sulfide oxidation (Z) for each sample was also determined by the inversion model (Kemeny & Torres, 2021). A high R value (approaching 1.0) indicates weathering is dominated by carbonates over silicates, while a high Z value indicates sulfuric acid playing a bigger role in weathering over carbonic acid. Overall, 0.98 (0.96 – 0.99) of weathering cations came from carbonate dissolution (**Table S7**), with the remaining fraction from silicate weathering calculated as (1-R) (Jenckes et al., 2024; Kemeny & Torres, 2021). Approximately 0.22 (0.20 – 0.22) of weathering acid came from sulfide oxidation at our study sites (**Table S7**). A plot of R versus Z for our dataset showed that all of the data fell within the bounds of short-term CO_2 consumption (**Figure 9**), with the acknowledgement that these samples would be net CO_2 neutral on timespans exceeding 10,000 years. By contrast, none of our data had a fraction of R so low that it was the product of pure silicate weathering or Z so high as to come from sulfide oxidation alone. In other words, though a smaller fraction of our data represented silicate weathering and sulfide oxidation, carbonate weathering by H_2CO_3 far outweighed them.

https://doi.org/10.5194/egusphere-2025-5020
Preprint. Discussion started: 16 October 2025

No clear pattern was discernable from assessing R and Z by sampling site (**Figure 9A**), with the exception of two BR2 datapoints that were characterized by relatively more silicate weathering at this mid-river site. While it should be noted that the majority of our data fell between a small range of R (~0.925 – 1.00), sites closer to their source glaciers across all rivers tended to have proportionally more carbonate-derived weathering products than downriver sites (**Figure 9B**). This conclusion supports the trends in $^{87}Sr/^{86}Sr$ and $\delta^{13}C$-DIC data described above. **Figure 9C**, presents the results of an ion only inversion model (i.e., excluding $^{34}S\text{-}SO_4$) to include winter data, for which $^{34}S\text{-}SO_4$ measurements were not collected. While the data hint at slightly elevated Z, indicating increased H_2SO_4 influence, during baseflow in autumn and winter compared to during spring and summer melt, seasonal means ± SD greatly overlapped and suggested no real differences between seasons (**Figure 9C**). Median and 25th and 75th percentile R and Z values for models with and without $^{34}S\text{-}SO_4$ can be found in **Table S7** and R versus Z color-coded by season for the inversion model with $^{34}S\text{-}SO_4$ is shown in **Figure S9** for comparison to **Figure 9C**.

https://doi.org/10.5194/egusphere-2025-5020
Preprint. Discussion started: 16 October 2025

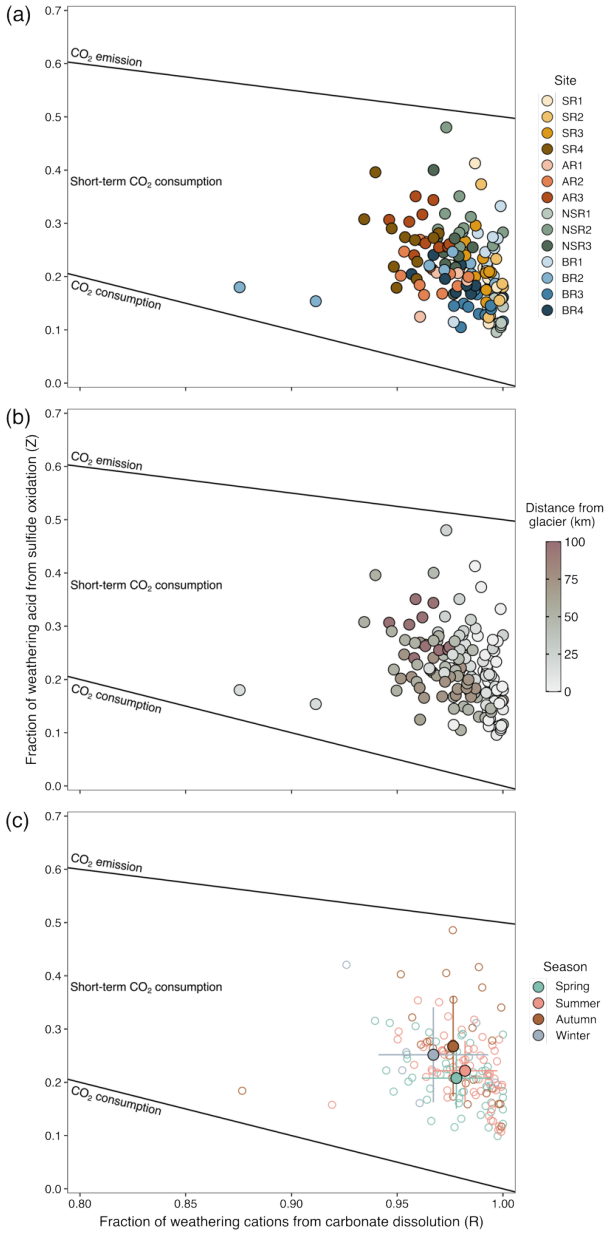

Figure 9. The fraction of weathering cations from carbonate dissolution (R) versus fraction of weathering acid from sulfide oxidation (Z) for each inversion model sample, color-coded by (A) site, (B) distance from glacier, and (C) season. $^{34}S\text{-}SO_4$ measurements were included in the inversion that produced (A) and (B), but not (C). Each datapoint is represented as a filled circle except in (C) where each datapoint is a hollow circle and mean seasonal data (± SD) is the filled circle.

https://doi.org/10.5194/egusphere-2025-5020
Preprint. Discussion started: 16 October 2025

3.4 Contribution from silicates and organic carbon to the DIC pool increased downriver

The strongest trend that emerged from the MEANDIR inversion model was that of distance from glacier having the greatest impact on the fraction of weathering cations from carbonate dissolution (**Figure 9B**). As a result, we then looked at the impact of distance from glacier on the relative percent of DIC from carbonate weathering, atmospheric $CO_{2(g)}$, OC, and silicate weathering in our study rivers (**Figure 10**). Sampling sites closest to their source glacier along each river transect had the highest percent of total DIC from carbonate weathering and the atmosphere, and the lowest percent of total DIC from OC (**Figure 10A**). However, we suspect that the mass balance model used herein likely overestimated DOC contributions to DIC concentration and isotope values at the most upriver sampling sites (i.e., SR1, SR2, NSR1, BR1) where DOC concentrations and yields were lowest (Serbu, St. Louis, et al., 2024) because it was not originally built for glacierized regions. The mass balance model we used (Voss et al., 2023) likely provided a better fit to our river systems which meandered from alpine to montane altitudinal life zones, with associated increases in temperatures, development of landscape soils, and potential allochthonous organic matter inputs into our rivers (S. P. Anderson, 2007; Robison et al., 2023). The sampling site with the highest percent of total DIC from OC was BR2 (**Figure 10**), which had the greatest relative percent wetland cover in its watershed of all sites (2.1 %), most of which bordered the river (**Figure 2**, **Table S2**). Otherwise, the percent total DIC that was derived from OC increased with distance downriver, as expected (**Figure 10A**) (Robison et al., 2023).

The percent total carbonate and atmospheric contributions to DIC was large (>50 %) at all sampling sites, but greatest (>75 %) at sites closest to their source glacier (**Figure 10A**), despite a likely overallocation of DOC contributions to percent of total DIC at these upriver sites. This was the case even at BR1 where $CO_{2(aq)}$ was near saturation (**Figure 3A**), emphasizing the importance of river topography, such as waterfalls, in mixing and gas equilibration. Sites closest to source glaciers had some of the highest total suspended solid concentrations (Serbu, St. Louis, et al., 2024), a consequence of subglacial abrasion and sediment expulsion with meltwaters (Comiti et al., 2019). Finely ground comminuted sediments facilitate weathering reactions (Brown et al., 1996) and carbonates tend to dominate weathering outputs (Blum et al., 1998) regardless of the dominant geology in a region. By comparison, Si concentrations and yields increased with distance

https://doi.org/10.5194/egusphere-2025-5020
Preprint. Discussion started: 16 October 2025

downriver (Serbu, St. Louis, et al., 2024). An increase in water temperature and terrestrially-sourced organic acids can stimulate weathering of silicates in surrounding soils, which may account for the higher Si concentrations at downriver sites (S. P. Anderson, 2005). Further, amorphous Si bound to suspended sediments has been found in glacial regions (Pryer et al., 2020), and the release of bound Si during transport along our rivers could have also contributed to higher Si concentrations at downriver sites.

The results of our mass balance support the interpretation that some of the increasing Si concentrations with distance downriver was caused by greater contributions from silicate weathering (**Figure 10B**). The proportion of DIC from silicate weathering is positively correlated to distance downriver after the most upriver sites ($R^2_{adj} = 0.109$, $p < 0.001$) (**Figure 10B**). Na^+ concentrations and yields support this conclusion as they increased downriver from glacier sources (Serbu, St. Louis, et al., 2024) in conjunction with an increase in modeled non-carbonate fractions (**Figure 10**). Our study provides new insights into how downriver shifts in temperature and organic matter availability may enhance silicate weathering processes.

https://doi.org/10.5194/egusphere-2025-5020
Preprint. Discussion started: 16 October 2025

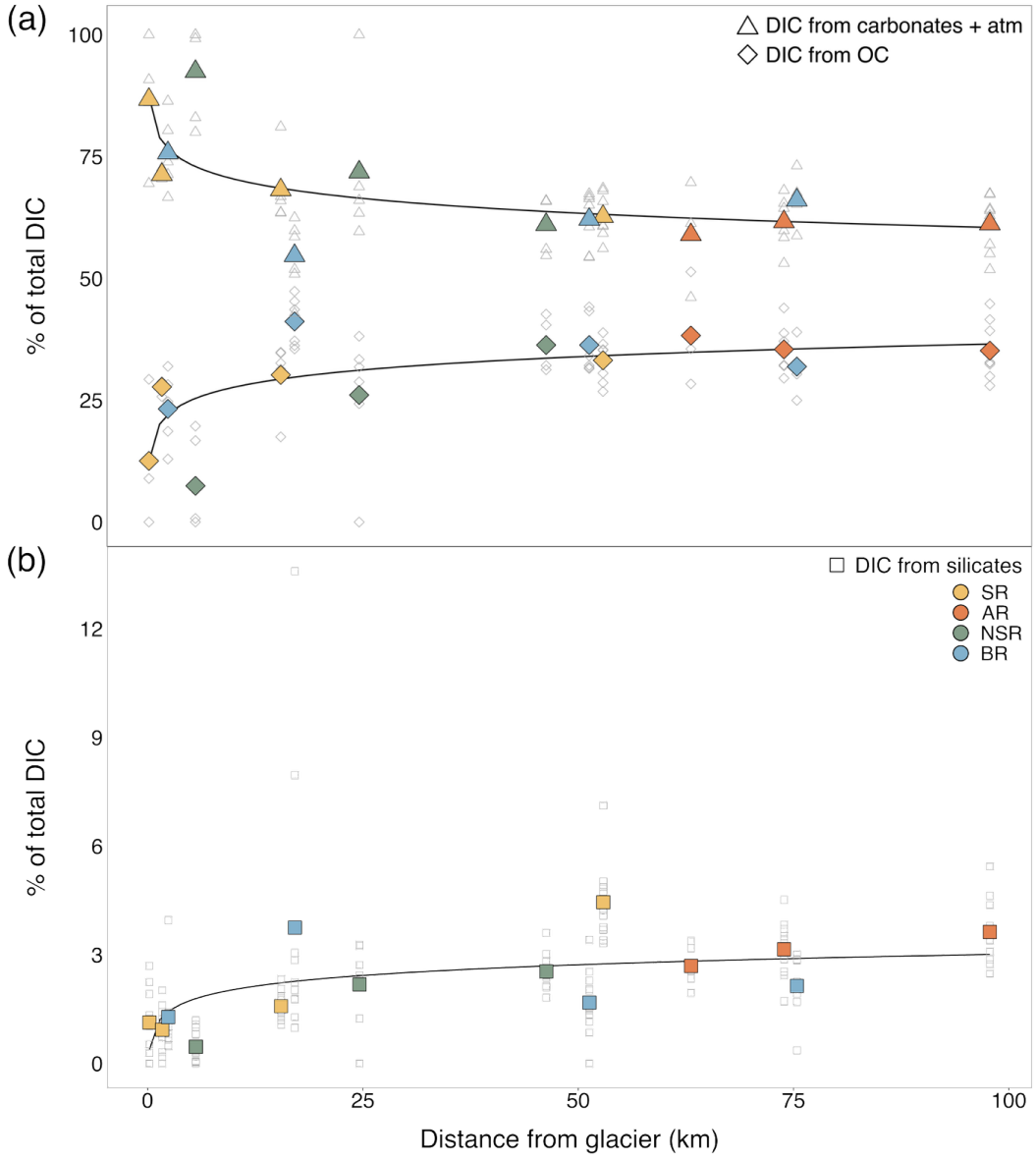

Figure 10. Percent of total dissolved inorganic carbon (DIC) derived from (A) carbonates and the atmosphere, organic carbon (OC), and (B) silicate weathering with downriver distance from source glaciers (km) along the Sunwapta (SR), Athabasca (AR), North Saskatchewan (NSR), and Bow (BR) rivers. Colored symbols are means, while individual datapoints from all seasons are seen outlined in grey.

https://doi.org/10.5194/egusphere-2025-5020
Preprint. Discussion started: 16 October 2025

4 Conclusions and the regional and global context

Geochemical weathering is especially prominent in glacierized environments due to the large amount of chemically reactive glacial flour being produced by subglacial abrasion of underlying bedrock (Tranter & Wadham, 2014). In general, however, we still know relatively little about how the type and magnitude of in-river geochemical weathering reactions change with distance downriver from their source glacier, or how this may change seasonally or interannually; this is likely due to the logistical difficulty of sampling glacier-fed rivers across space and time in Arctic and alpine environments. As far as we are aware, this study presents the first assessment of geochemical weathering data across all seasons (spring, summer, autumn, winter) from glacierized river transects (0.2 to 100 km) that meander through alpine, subalpine, and montane altitudinal life zones. The underlying ecological complexity of our mid-latitude alpine study region encouraged us to investigate geochemical weathering through various means. Instantaneous CO_2 fluxes showed that net CO_2 consumption from the atmosphere at sampling sites closest to the source glaciers exceeded that of other global landscapes, such as tropical forests, many times over (IPCC, 2001). However, fluxes quickly became neutral or even slightly emissive to the atmosphere at downriver sites, including after a proglacial lake (i.e., SR2) that acted as a sediment sink on the landscape (Serbu, St. Louis, et al., 2024). Basic river geochemistry and a large suite of isotope signatures ($^{87}Sr/^{86}Sr$, $\delta^{34}S$-SO_4, $\delta^{18}O$-SO_4, $\delta^{13}C$-PIC, $\delta^{13}C$-DIC, and $\Delta^{14}C$-DIC) analyzed in this study aided in elucidating that calcium bicarbonate dominating the ion pool across all sites and weathering dynamics changed across space and time. This was supported by an inversion weathering model that determined the proportion of ions that came from precipitation, evaporite, carbonate, silicate, and pyrite endmembers (Kemeny & Torres, 2021). The inversion model suggested a dominance of H_2CO_3-carbonate weathering with a trend of increasing silicate weathering with distance from glacier. Because the downriver reaches of the Sunwapta-Athabasca, North Saskatchewan, and Bow are within alpine, subalpine, and montane altitudinal life zones, a downriver increase in allochthonous OC to the lotic system is assumed. As such, we additionally employed an inclusive inorganic-organic carbon mass balance model (Voss et al., 2023), which is atypical in glacierized watersheds, to track the proportions of riverine DIC that resulted from carbonate weathering and the atmosphere, the respiration of OC, and silicate weathering. These results reinforce a relative increase in OC and silicate weathering derived DIC with increasing

https://doi.org/10.5194/egusphere-2025-5020
Preprint. Discussion started: 16 October 2025

distance from glacier. Overall, using these multiple lines of evidence, we illustrate that distance from glacier was a key determinant of the type and magnitude of in-river geochemical weathering as the rivers meandered through alpine to montane altitudinal life zones, with river, season, and year being less important determinants.

The implications of our research are noteworthy at both the regional and global scale. The alpine glaciers of the Canadian Rocky Mountains that feed our study rivers are relatively small in size (Radić et al., 2014; Rounce et al., 2023) and are therefore particularly sensitive to changes in temperature and atmospheric conditions (Menounos et al., 2019; Rounce et al., 2023). On the eastern slopes, glacier volume is projected to decline 80 – 90 % by 2100 with subsequent changes to the volume and timing of meltwater and biogeochemical inputs into receiving rivers (Clarke et al., 2015; Radić et al., 2014). This has serious consequences for freshwater availability to downriver ecosystems and human communities (S. Anderson & Radić, 2020; Schindler & Donahue, 2006), and will also importantly impact the in situ geochemical processes that are occurring within these rivers, as suggested by our study.

Globally, non-icesheet glaciers only cover an area of about 706,000 km^2 (Zemp et al., 2019). However, these glaciers are undergoing extreme thinning and mass loss (Hugonnet et al., 2021), leading to a decrease in the glacierized area of land and increase in area of new land exposed to subaerial weathering. The results from our study offer insight into how changes in the type and magnitude of geochemical weathering may occur as new landscape area is exposed. On a shorter timescale, land will be laden with comminuted sediment left behind by glacier abrasion, exposed to the atmosphere for the first time, and thus be prone to geochemical reactions. The type of weathering is likely to initially be the fast-acting carbonate weathering and sulfide oxidation-carbonate dissolution (Torres et al., 2017). On a longer timescale, increases in temperature, soil development, and the succession of vegetation in these formerly barren environments will promote the production of autochthonous OC and, potentially, silicate weathering (S. P. Anderson et al., 2000).

The greening of mountains is happening everywhere on Earth (e.g., Choler et al., 2025; Grimes et al., 2024), making it critical to investigate patterns in geochemical weathering spatiotemporally

https://doi.org/10.5194/egusphere-2025-5020
Preprint. Discussion started: 16 October 2025

across diverse glacierized regions for the benefit of global predictive models. The results from our study offer insight into how changes in the type and magnitude of geochemical weathering may occur concurrently with the greening of mountains as new landscape area is exposed. Our field-based observations of geochemical weathering are vital to the development and ground-truthing of regional and global carbon climate models. Given the collective effort in producing the dataset used herein, we also encourage others to mine and analyze it in ways we did not here.

5 Data availability

All datasets used in this work are open source. The datasets that form the basis of this manuscript were submitted to the PANGAEA repository (Felden et al., 2023) and are available as "Physicochemical, particulate matter, temperature, and hydrological data sets collected from climate-threatened glacial river headwaters on the eastern slopes of the Canadian Rocky Mountains (2019–2021)" at Serbu et al., (2023), "Weathering dataset collected from climate-threatened glacial river headwaters on the eastern slopes of the Canadian Rocky Mountains (2019-2021)" at Serbu, Tank, et al., (2024), and "Organic carbon concentration, absorbance and fluorescent characteristics, and isotopic composition of river water sourced from four glacially-fed rivers in the Canadian Rocky Mountains (2019-2021) " at Drapeau et al., 2025a. Map base layers produced by Alberta Environment and Parks are from Alberta ArcHydro Phase 2 Data (https:// open.alberta.ca/opendata/gda-d22f5906-358e-47b9-9259-02702932a7a0#summary; Alberta Environment and Parks, 2018). Land cover classes for each sampling site were obtained with the 2010 ABMI Wall-to-Wall Land Cover Inventory (https://abmi.ca/home/data-analytics/da-top/da-product-overview/Data-Archive/Land-Cover. html; Alberta Biodiversity Monitoring Institute, 2010) and the 2021 ABMI Wetland Inventory (https://abmi. ca/home/data-analytics/da-top/da-product-overview/Advanced-Landcover-Prediction-and-Habitat-Assessment--ALPHA--Products/ABMI-Wetland-Inventory.html; Alberta Biodiversity Monitoring Institute, 2021). Lastly, discharge measures from the National Water Data Archive: HYDAT were obtained by Water Survey of Canada and were invaluable to this study (https://www.canada.ca/en/environment-climate-change/services/water-overview/quantity/monitoring/survey/data-products-services/national-archive-hydat.html; Water Survey of Canada, 2021).

https://doi.org/10.5194/egusphere-2025-5020
Preprint. Discussion started: 16 October 2025

6 Author contribution

Conceptualization was by JAS, VLSL, SET, and BPE; formal analysis was by JAS, XS, and CAE; funding acquisition was by VLSL and SET; investigation was by JAS, VLSL, SET, CAE; resources were by VLSL, SET, and BPE; supervision was by VLSL and BPE; visualization was by JAS, XS, and CAE; original draft preparation was by JAS; and writing (review and editing) was by all authors.

7 Competing interests

The authors declare that they have no conflict of interest.

8 Acknowledgements

Data collected via fieldwork was approved under permits JNP-2018-29597 (Jasper National Park) and LL-2019-32266 (Banff National Park). Thank you Hayley F. Drapeau, Sydney J. A. Enns, and Janelle E. Flett for your critical role in sample collection and analysis. We would also like to thank the Biogeochemical Analytical Service Laboratory (BASL; University of Alberta), The Environmental Isotope Laboratory (EIL; University of Waterloo), Ján Veizer Stable Isotope Laboratory (University of Ottawa), the WHOI Plasma Facility (Woods Hole Oceanographic Institution), National Ocean Sciences Mass Spectrometry Facility (NOSAMS; Woods Hole Oceanographic Institution) and André E. Lalonde Accelerator Mass Spectrometry Laboratory (AEL-AMS; University of Ottawa) for their role in the laboratory analysis of our samples. Thank you to Shelby Stenerson for adapting Figure 1D and Studio X Design for creating Figure 2. Funding was provided by the Canadian Mountain Network (grant holder VLSL), Natural Sciences and Engineering Research Council of Canada (NSERC) Discovery Grant (grant holder VLSL), the Campus Alberta Innovation Program (Chairs SET and Maya P. Bhatia), and the Alberta Conservation Association Biodiversity Grant (grant holder JAS). JAS was funded through an NSERC CGS-M, NSERC PGS-D, Henry Kroeger Memorial Graduate Scholarship, and Government of Alberta Women in STEM Scholarship, and was a Guest Student at WHOI for parts of this study. We acknowledge that the University of Alberta is on Treaty 6 Territory and fieldwork

https://doi.org/10.5194/egusphere-2025-5020
Preprint. Discussion started: 16 October 2025

was conducted on Treaty 7 and 8 Territories. Jasper and Banff National Parks are located on the lands of the Ktunaxa ʔamakʔis (Ktunaxa), As'in'i'wa'chi Niy'yaw Askiy (Rocky Mountain Cree), Îyãhé Nakón mąkóce (Stoney), Niitsítpiis-stahkoii ᖽᐧᒧ·ᑯ· ᓴᙱᐧ (Blackfoot / Niitsítapi ᖽᐧᒧ·ᒣᑯ), Secwepemcúl'ecw (Secwépemc), Tsuut'ina, Michif Piyii (Métis), and Mountain Métis people.

References

Alberta Biodiversity Monitoring Institute. (2010). *ABMI Wall-to-Wall Land Cover Inventory*. https://abmi.ca/home/data-analytics/da-top/da-product-overview/Data-Archive/Land-Cover.html

Alberta Biodiversity Monitoring Institute. (2021). *ABMI Wetland Inventory*. https://abmi.ca/home/data-analytics/da-top/da-product-overview/Advanced-Landcover-Prediction-and-Habitat-Assessment--ALPHA--Products/ABMI-Wetland-Inventory.html

Alberta Environment and Parks. (2017). *Alberta Provincial Digital Elevation Model* [Computer software]. Alberta Government.

Alberta Environment and Parks. (2018). *Alberta ArcHydro Phase 2 Data*. https://open.alberta.ca/opendata/gda-d22f5906-358e-47b9-9259-02702932a7a0#summary

American Public Health Association, American Water Works Association, & Water Environment Federation. (2023a). Method 3125-Metals by Inductively Coupled Plasma-Mass Spectrometry (ICP-MS). In W. C. Lipps, T. E. Baxter, & E. Braun-Howland (Eds.), *Standard Methods For the Examination of Water and Wastewater* (24th ed.). APHA Press. https://doi.org/10.2105/smww.2882.048

American Public Health Association, American Water Works Association, & Water Environment Federation. (2023b). Method 4500-SiO2 (Silica). In W. C. Lipps, T. E.

https://doi.org/10.5194/egusphere-2025-5020
Preprint. Discussion started: 16 October 2025

Baxter, & E. Braun-Howland (Eds.), *Standard Methods For the Examination of Water and Wastewater* (24th ed.). APHA Press. https://doi.org/10.2105/SMWW.2882.095

American Public Health Association, American Water Works Association, & Water Environment Federation. (2023c). Method 5310—TOC (Total organic carbon). In W. C. Lipps, T. E. Baxter, & E. Braun-Howland (Eds.), *Standard Methods for the Examination of Water and Wastewater* (24th ed.). APHA Press. https://doi.org/10.2105/SMWW.2882.104

Anderson, S. P. (2005). Glaciers show direct linkage between erosion rate and chemical weathering fluxes. *Geomorphology*, *67*(1–2), 147–157. https://doi.org/10.1016/j.geomorph.2004.07.010

Anderson, S. P. (2007). Biogeochemistry of glacial landscape systems. *Annual Review of Earth and Planetary Sciences*, *35*(1), 375–399. https://doi.org/10.1146/annurev.earth.35.031306.140033

Anderson, S. P., Drever, J. I., Frost, C. D., & Holden, P. (2000). Chemical weathering in the foreland of a retreating glacier. *Geochimica et Cosmochimica Acta*, *64*(7), 1173–1189. https://doi.org/10.1016/S0016-7037(99)00358-0

Anderson, S. P., Drever, J. I., & Humphrey, N. F. (1997). Chemical weathering in glacial environments. *Geology*, *25*(5), 399–402.

Anderson, S., & Radić, V. (2020). Identification of local water resource vulnerability to rapid deglaciation in Alberta. *Nature Climate Change*, *10*(10), 933–938. https://doi.org/10.1038/s41558-020-0863-4

Andrews, M. G., & Jacobson, A. D. (2018). Controls on the solute geochemistry of subglacial discharge from the Russell Glacier, Greenland Ice Sheet determined by radiogenic and

https://doi.org/10.5194/egusphere-2025-5020
Preprint. Discussion started: 16 October 2025

stable Sr isotope ratios. *Geochimica et Cosmochimica Acta*, *239*, 312–329. https://doi.org/10.1016/j.gca.2018.08.004

Arendt, C. A., Stevenson, E. I., & Aciego, S. M. (2016). Hydrologic controls on radiogenic Sr in meltwater from an alpine glacier system: Athabasca Glacier, Canada. *Applied Geochemistry*, *69*, 42–49. https://doi.org/10.1016/j.apgeochem.2016.04.002

Aucour, A.-M., Sheppard, S. M. F., Guyomar, O., & Wattelet, J. (1999). Use of 13C to trace origin and cycling of inorganic carbon in the Rhone river system. *Chemical Geology*, *159*, 87–105.

Bade, D. L. (2009). Gas Exchange at the Air–Water Interface. In *Encyclopedia of Inland Waters* (pp. 70–78). Elsevier. https://doi.org/10.1016/B978-012370626-3.00213-1

Bagshaw, E. A., Wadham, J. L., Tranter, M., Beaton, A. D., Hawkings, J. R., Lamarche-Gagnon, G., & Mowlem, M. C. (2021). Measuring pH in low ionic strength glacial meltwaters using ion selective field effect transistor (ISFET) technology. *Limnology and Oceanography: Methods*, *19*(3), 222–233. https://doi.org/10.1002/lom3.10416

Berner, R. A. (1992). Weathering, plants, and the long-term carbon cycle. *Geochimica et Cosmochimica Acta*, *56*(8), 3225–3231. https://doi.org/10.1016/0016-7037(92)90300-8

Bish, D. L., & Plötze, M. (2010). X-Ray Powder Diffraction with Emphasis on Qualitative and Quantatative Analysis in Industrial Mineralogy. In *Advances In The Characterization of Industrial Minerals* (Vol. 9). European Mineralogical Union.

Blum, J. D., & Erel, Y. (1995). A silicate weathering mechanism linking increases in marine 875r/865r with global glaciation. *Nature*, *373*, 415–418.

Blum, J. D., Gazis, C. A., Jacobson, A. D., & Page Chamberlain, C. (1998). Carbonate versus silicate weathering in the Raikhot watershed within the High Himalayan Crystalline

https://doi.org/10.5194/egusphere-2025-5020
Preprint. Discussion started: 16 October 2025

Series. *Geology*, *26*(5), 411. https://doi.org/10.1130/0091-7613(1998)026%253C0411:CVSWIT%253E2.3.CO;2

Bowman, M. F., Chambers, P. A., & Schindler, D. W. (2005). Epilithic algal abundance in relation to anthropogenic changes in phosphorus bioavailability and limitation in mountain rivers. *Canadian Journal of Fisheries and Aquatic Sciences*, *62*(1), 174–184. https://doi.org/10.1139/f04-244

Bowman, M. F., Chambers, P. A., & Schindler, D. W. (2007). Constraints on benthic algal response to nutrient addition in oligotrophic mountain rivers. *River Research and Applications*, *23*(8), 858–876. https://doi.org/10.1002/rra.1025

Brown, G. H., Tranter, M., & Sharp, M. J. (1996). Experimental investigations of the weathering of suspended sediment bu alpine glacial meltwater. *Hydrological Processes*, *10*(4), 579–597. https://doi.org/10.1002/(SICI)1099-1085(199604)10:4%253C579::AID-HYP393%253E3.0.CO;2-D

Burke, A., Present, T. M., Paris, G., Rae, E. C. M., Sandilands, B. H., Gaillardet, J., Peucker-Ehrenbrink, B., Fischer, W. W., McClelland, J. W., Spencer, R. G. M., Voss, B. M., & Adkins, J. F. (2018). Sulfur isotopes in rivers: Insights into global weathering budgets, pyrite oxidation, and the modern sulfur cycle. *Earth and Planetary Science Letters*, *496*, 168–177. https://doi.org/10.1016/j.epsl.2018.05.022

Carey, J. C., & Fulweiler, R. W. (2013). Watershed land use alters riverine silica cycling. *Biogeochemistry*, *113*(1–3), 525–544. https://doi.org/10.1007/s10533-012-9784-2

Choler, P., Bayle, A., Fort, N., & Gascoin, S. (2025). Waning snowfields have transformed into hotspots of greening within the alpine zone. *Nature Climate Change*, *15*(1), 80–85. https://doi.org/10.1038/s41558-024-02177-x

https://doi.org/10.5194/egusphere-2025-5020
Preprint. Discussion started: 16 October 2025

Comiti, F., Mao, L., Penna, D., Dell'Agnese, A., Engel, M., Rathburn, S., & Cavalli, M. (2019). Glacier melt runoff controls bedload transport in Alpine catchments. *Earth and Planetary Science Letters*, *520*, 77–86. https://doi.org/10.1016/j.epsl.2019.05.031

de Montety, V., Martin, J. B., Cohen, M. J., Foster, C., & Kurz, M. J. (2011). Influence of diel biogeochemical cycles on carbonate equilibrium in a karst river. *Chemical Geology*, S0009254111000052. https://doi.org/10.1016/j.chemgeo.2010.12.025

Deuerling, K. M., Martin, J. B., Martin, E. E., Abermann, J., Myreng, S. M., Petersen, D., & Rennermalm, Å. K. (2019). Chemical weathering across the western foreland of the Greenland Ice Sheet. *Geochimica et Cosmochimica Acta*, *245*, 426–440. https://doi.org/10.1016/j.gca.2018.11.025

Dixon, J. C., & Thorn, C. E. (2005). Chemical weathering and landscape development in mid-latitude alpine environments. *Geomorphology*, *67*(1–2), 127–145. https://doi.org/10.1016/j.geomorph.2004.07.009

Donnini, M., Frondini, F., Probst, J.-L., Probst, A., Cardellini, C., Marchesini, I., & Guzzetti, F. (2016). Chemical weathering and consumption of atmospheric carbon dioxide in the Alpine region. *Global and Planetary Change*, *136*, 65–81. https://doi.org/10.1016/j.gloplacha.2015.10.017

Drapeau, H. F., Tank, S. E., Cavaco, M., Serbu, J. A., St. Louis, V. L., & Bhatia, M. P. (2025a). Organic carbon concentration, absorbance and fluorescent characteristics, and isotopic composition of river water sourced from four glacially-fed rivers in the Canadian Rocky Mountains (2019-2021) [dataset]. *PANGAEA*. https://doi.pangaea.de/10.1594/PANGAEA.975984

https://doi.org/10.5194/egusphere-2025-5020
Preprint. Discussion started: 16 October 2025

Drapeau, H. F., Tank, S. E., Cavaco, M., Serbu, J. A., St. Louis, V. L., & Bhatia, M. P. (2025b). Shifts in organic matter character and microbial assemblages from glacial headwaters to downstream reaches in the Canadian Rocky Mountain. *Biogeosciences Discussions*. https://doi.org/10.5194/bg-2023-121

ESRI. (2023). *ArcGIS Desktop*.

Felden, J., Möller, L., Schindler, U., Huber, R., Schumacher, S., Koppe, R., Diepenbroek, M., & Glöckner, F. O. (2023). PANGAEA - Data Publisher for Earth & Environmental Science. *Scientific Data*, *10*(1), 347–347. https://doi.org/10.1038/s41597-023-02269-x

Gadd, B. (2009). *Handbook of the Canadian Rockies*. Corex Press.

Gaillardet, J., Dupré, B., Louvat, P., & Allègre, C. J. (1999). Global silicate weathering and CO_2 consumption rates deduced from the chemistry of large rivers. *Chemical Geology*, *159*(1–4), 3–30. https://doi.org/10.1016/S0009-2541(99)00031-5

Gaines, R. R., Hammarlund, E. U., Hou, X., Qi, C., Gabbott, S. E., Zhao, Y., Peng, J., & Canfield, D. E. (2012). Mechanism for Burgess Shale-type preservation. *Proceedings of the National Academy of Sciences*, *109*(14), 5180–5184. https://doi.org/10.1073/pnas.1111784109

Graly, J. A., Humphrey, N. F., Landowski, C. M., & Harper, J. T. (2014). Chemical weathering under the Greenland Ice Sheet. *Geology*, *42*(6), 551–554. https://doi.org/10.1130/G35370.1

Grimes, M., Carrivick, J. L., Smith, M. W., & Comber, A. J. (2024). Land cover changes across Greenland dominated by a doubling of vegetation in three decades. *Scientific Reports*, *14*(1), 3120. https://doi.org/10.1038/s41598-024-52124-1

https://doi.org/10.5194/egusphere-2025-5020
Preprint. Discussion started: 16 October 2025

Hall, R. O., & Ulseth, A. J. (2020). Gas exchange in streams and rivers. *WIREs Water*, *7*(1), e1391. https://doi.org/10.1002/wat2.1391

Hayashi, M. (2020). Alpine hydrogeology: The critical role of groundwater in sourcing the headwaters of the world. *Groundwater*, *58*(4), 498–510. https://doi.org/10.1111/gwat.12965

Hindshaw, R. S., Rickli, J., Leuthold, J., Wadham, J., & Bourdon, B. (2014). Identifying weathering sources and processes in an outlet glacier of the Greenland Ice Sheet using Ca and Sr isotope ratios. *Geochimica et Cosmochimica Acta*, *145*, 50–71. https://doi.org/10.1016/j.gca.2014.09.016

Hodson, A., Tranter, M., & Vatne, G. (2000). Contemporary rates of chemical denudation and atmospheric CO_2 sequestration in glacier basins: An Arctic perspective. *Earth Surface Processes and Landforms*, *25*, 1447–1471.

Horgby, Å., Canadell, M. B., Ulseth, A. J., Vennemann, T. W., & Battin, T. J. (2019). High-resolution spatial sampling identifies groundwater as driver of CO_2 dynamics in an alpine stream network. *Journal of Geophysical Research: Biogeosciences*, *124*(7), 1961–1976. https://doi.org/10.1029/2019JG005047

Hugonnet, R., McNabb, R., Berthier, E., Menounos, B., Nuth, C., Girod, L., Farinotti, D., Huss, M., Dussaillant, I., Brun, F., & Kääb, A. (2021). Accelerated global glacier mass loss in the early twenty-first century. *Nature*, *592*(7856), 726–731. https://doi.org/10.1038/s41586-021-03436-z

IPCC. (2001). *Climate Change 2001: The Scientific Basis*.

https://doi.org/10.5194/egusphere-2025-5020
Preprint. Discussion started: 16 October 2025

Ishikawa, N. F., Doi, H., & Finlay, J. C. (2012). Global meta-analysis for controlling factors on carbon stable isotope ratios of lotic periphyton. *Oecologia*, *170*(2), 541–549. https://doi.org/10.1007/s00442-012-2308-x

Isson, T. T., Planavsky, N. J., Coogan, L. A., Stewart, E. M., Ague, J. J., Bolton, E. W., Zhang, S., McKenzie, N. R., & Kump, L. R. (2020). Evolution of the global carbon cycle and climate regulation on Earth. *Global Biogeochemical Cycles*, *34*(2), e2018GB006061. https://doi.org/10.1029/2018GB006061

Jenckes, J., Muñoz, S., Ibarra, D. E., Boutt, D. F., & Munk, L. A. (2024). Geochemical weathering variability in high latitude watersheds of the Gulf of Alaska. *Journal of Geophysical Research: Earth Surface*, *129*(3), e2023JF007284. https://doi.org/10.1029/2023JF007284

Johnson, J. E., Gerpheide, A., Lamb, M. P., & Fischer, W. W. (2014). O_2 constraints from Paleoproterozoic detrital pyrite and uraninite. *Geological Society of America Bulletin*, *126*(5–6), 813–830. https://doi.org/10.1130/B30949.1

Johnson, M. S., Billett, M. F., Dinsmore, K. J., Wallin, M., Dyson, K. E., & Jassal, R. S. (2010). Direct and continuous measurement of dissolved carbon dioxide in freshwater aquatic systems—Method and applications. *Ecohydrology*, *3*(1), 68–78. https://doi.org/10.1002/eco.95

Kemeny, P. C., & Torres, M. A. (2021). Presentation and applications of mixing elements and dissolved isotopes in rivers (MEANDIR), a customizable MATLAB model for Monte Carlo inversion of dissolved river chemistry. *American Journal of Science*, *321*(5), 579–642. https://doi.org/10.2475/05.2021.03

https://doi.org/10.5194/egusphere-2025-5020
Preprint. Discussion started: 16 October 2025

Kemeny, P. C., Torres, M. A., Lamb, M. P., Webb, S. M., Dalleska, N., Cole, T., Hou, Y., Marske, J., Adkins, J. F., & Fischer, W. W. (2021). Organic sulfur fluxes and geomorphic control of sulfur isotope ratios in rivers. *Earth and Planetary Science Letters*, *562*, 116838. https://doi.org/10.1016/j.epsl.2021.116838

Kempe, S. (1988). Freshwater Carbon and the Weathering Cycle. In A. Lerman & M. Meybeck (Eds.), *Physical and Chemical Weathering in Geochemical Cycles* (pp. 197–223). Springer Netherlands. https://doi.org/10.1007/978-94-009-3071-1_10

Khadka, M. B., Martin, J. B., & Jin, J. (2014). Transport of dissolved carbon and CO_2 degassing from a river system in a mixed silicate and carbonate catchment. *Journal of Hydrology*, *513*, 391–402. https://doi.org/10.1016/j.jhydrol.2014.03.070

Li, S.-L., Calmels, D., Han, G., Gaillardet, J., & Liu, C.-Q. (2008). Sulfuric acid as an agent of carbonate weathering constrained by $\delta 13C_{DIC}$: Examples from Southwest China. *Earth and Planetary Science Letters*, *270*(3–4), 189–199. https://doi.org/10.1016/j.epsl.2008.02.039

Li, X., Wang, N., Ding, Y., Hawkings, J. R., Yde, J. C., Raiswell, R., Liu, J., Zhang, S., Kang, S., Wang, R., Liu, Q., Liu, S., Bol, R., You, X., & Li, G. (2022). Globally elevated chemical weathering rates beneath glaciers. *Nature Communications*, *13*(1), 407. https://doi.org/10.1038/s41467-022-28032-1

Liu, Z., Dreybrodt, W., & Liu, H. (2011). Atmospheric CO_2 sink: Silicate weathering or carbonate weathering? *Applied Geochemistry*, *26*, S292–S294. https://doi.org/10.1016/j.apgeochem.2011.03.085

Mackenzie, F. T., & Garrels, R. M. . (1966). Chemical mass balance between rivers and oceans. *American Journal of Science*, *264*, 507–525.

https://doi.org/10.5194/egusphere-2025-5020
Preprint. Discussion started: 16 October 2025

Mancini, D., Dietze, M., Müller, T., Jenkin, M., Miesen, F., Roncoroni, M., Nicholas, A. P., & Lane, S. N. (2023). Filtering of the signal of sediment export from a glacier by its proglacial forefield. *Geophysical Research Letters*, *50*(21), e2023GL106082. https://doi.org/10.1029/2023GL106082

Martin, J. B. (2017). Carbonate minerals in the global carbon cycle. *Chemical Geology*, *449*, 58–72. https://doi.org/10.1016/j.chemgeo.2016.11.029

Marwick, T. R., Tamooh, F., Teodoru, C. R., Borges, A. V., Darchambeau, F., & Bouillon, S. (2015). The age of river-transported carbon: A global perspective. *Global Biogeochemical Cycles*, *29*(2), 122–137. https://doi.org/10.1002/2014GB004911

Menounos, B., Hugonnet, R., Shean, D., Gardner, A., Howat, I., Berthier, E., Pelto, B., Tennant, C., Shea, J., Noh, M., Brun, F., & Dehecq, A. (2019). Heterogeneous changes in western North American glaciers linked to decadal variability in zonal wind strength. *Geophysical Research Letters*, *46*(1), 200–209. https://doi.org/10.1029/2018GL080942

Meybeck, M. (1993). Riverine transport of atmospheric carbon: Sources, global typology and budget. *Water, Air, & Soil Pollution*, *70*(1–4), 443–463.

Mountjoy, E. W. (1962). *Mount Robson (southeast) map-area, Rocky Mountains of Alberta and British Columbia, 83E/SE* [Map]. Geological Survey of Canada. https://doi.org/10.4095/101251

Muñoz, S., Jenckes, J., Ramos, E. J., Munk, L. A., & Ibarra, D. E. (2024). Hydrologic and landscape controls on rock weathering along a glacial gradient in South Central Alaska, USA. *Journal of Geophysical Research: Earth Surface*, *129*(3), e2023JF007255. https://doi.org/10.1029/2023JF007255

https://doi.org/10.5194/egusphere-2025-5020
Preprint. Discussion started: 16 October 2025

Murseli, S., Middlestead, P., St-Jean, G., Zhao, X., Jean, C., Crann, C. A., Kieser, W. E., & Clark, I. D. (2019). The preparation of water (DIC, DOC) and Gas (CO_2, CH_4) samples for radiocarbon analysis at AEL-AMS, Ottawa, Canada. *Radiocarbon*, *61*(5), 1563–1571. https://doi.org/10.1017/RDC.2019.14

Nanus, L., Campbell, D. H., Ingersoll, G. P., Clow, D. W., & Alisa Mast, M. (2003). Atmospheric deposition maps for the Rocky Mountains. *Atmospheric Environment*, *37*(35), 4881–4892. https://doi.org/10.1016/j.atmosenv.2003.08.024

Pana, D. I., & Elgr, R. (2013). *Geology of the Alberta Rocky Mountains and Foothills (Map No. 560)* [Map]. Alberta Geological Survey.

Paznekas, A., & Hayashi, M. (2016). Groundwater contribution to winter streamflow in the Canadian Rockies. *Canadian Water Resources Journal / Revue Canadienne Des Ressources Hydriques*, *41*(4), 484–499. https://doi.org/10.1080/07011784.2015.1060870

Peucker-Ehrenbrink, B., & Fiske, G. J. (2019). A continental perspective of the seawater 87Sr/86Sr record: A review. *Chemical Geology*, *510*, 140–165. https://doi.org/10.1016/j.chemgeo.2019.01.017

Price, R. A. (2000). *The Southern Canadian Rockies: Evolution of a Foreland Thrust and Fold Belt (Field Trip Guidebook)*. Canadian Society of Petroleum Geologists. DOI: 10.13140/2.1.2910.2887

Pryer, H. V., Hawkings, J. R., Wadham, J. L., Robinson, L. F., Hendry, K. R., Hatton, J. E., Kellerman, A. M., Bertrand, S., Gill-Olivas, B., Marshall, M. G., Brooker, R. A., Daneri, G., & Häussermann, V. (2020). The influence of glacial cover on riverine silicon and iron exports in Chilean Patagonia. *Global Biogeochemical Cycles*, *34*(12), e2020GB006611. https://doi.org/10.1029/2020GB006611

https://doi.org/10.5194/egusphere-2025-5020
Preprint. Discussion started: 16 October 2025

Radić, V., Bliss, A., Beedlow, A. C., Hock, R., Miles, E., & Cogley, J. G. (2014). Regional and global projections of twenty-first century glacier mass changes in response to climate scenarios from global climate models. *Climate Dynamics*, *42*(1–2), 37–58. https://doi.org/10.1007/s00382-013-1719-7

Raiswell, R. (1984). Chemical models of solute acquisition in glacial melt waters. *Journal of Glaciology*, *30*(104), 49–57. https://doi.org/10.3189/S0022143000008480

Raymond, P. A., Hartmann, J., Lauerwald, R., Sobek, S., McDonald, C., Hoover, M., Butman, D., Striegl, R., Mayorga, E., Humborg, C., Kortelainen, P., Dürr, H., Meybeck, M., Ciais, P., & Guth, P. (2013). Global carbon dioxide emissions from inland waters. *Nature*, *503*(7476), 355–359. https://doi.org/10.1038/nature12760

Raymond, P. A., Zappa, C. J., Butman, D., Bott, T. L., Potter, J., Mulholland, P., Laursen, A. E., McDowell, W. H., & Newbold, D. (2012). Scaling the gas transfer velocity and hydraulic geometry in streams and small rivers. *Limnology and Oceanography: Fluids and Environments*, *2*(1), 41–53. https://doi.org/10.1215/21573689-1597669

Relph, K. E., Stevenson, E. I., Turchyn, A. V., Antler, G., Bickle, M. J., Baronas, J. J., Darby, S. E., Parsons, D. R., & Tipper, E. T. (2021). Partitioning riverine sulfate sources using oxygen and sulfur isotopes: Implications for carbon budgets of large rivers. *Earth and Planetary Science Letters*, *567*, 116957. https://doi.org/10.1016/j.epsl.2021.116957

Robison, A. L., Deluigi, N., Rolland, C., Manetti, N., & Battin, T. (2023). Glacier loss and vegetation expansion alter organic and inorganic carbon dynamics in high-mountain streams. *Biogeosciences*, *20*(12), 2301–2316. https://doi.org/10.5194/bg-20-2301-2023

Rounce, D. R., Hock, R., Maussion, F., Hugonnet, R., Kochtitzky, W., Huss, M., Berthier, E., Brinkerhoff, D., Compagno, L., Copland, L., Farinotti, D., Menounos, B., & McNabb, R.

https://doi.org/10.5194/egusphere-2025-5020
Preprint. Discussion started: 16 October 2025

W. (2023). Global glacier change in the 21st century: Every increase in temperature matters. *Science*, *379*(6627), 78–83. https://doi.org/10.1126/science.abo1324

Rubey, W. W. (1951). Geologic history of sea water: An attempt to state the problem. *Bulletin of the Geological Society of America*, *62*, 1111–1148.

Schindler, D. W., & Donahue, W. F. (2006). An impending water crisis in Canada's western prairie provinces. *Proceedings of the National Academy of Sciences*, *103*(19), 7210–7216. https://doi.org/10.1073/pnas.0601568103

Schlesinger, W. H., & Bernhardt, E. S. (2013). *Biogeochemistry: An Analysis of Global Change* (3rd ed.). Elsevier Inc.

Scribner, C. A., Martin, E. E., Martin, J. B., Deuerling, K. M., Collazo, D. F., & Marshall, A. T. (2015). Exposure age and climate controls on weathering in deglaciated watersheds of western Greenland. *Geochimica et Cosmochimica Acta*, *170*, 157–172. https://doi.org/10.1016/j.gca.2015.08.008

Serbu, J. A., St. Louis, V. L., Emmerton, C. A., Tank, S. E., Criscitiello, A. S., Silins, U., Bhatia, M. P., Cavaco, M. A., Christenson, C., Cooke, C. A., Drapeau, H. F., Enns, S. J. A., Flett, J. E., Holland, K. M., Lavallee-Whiffen, J., Ma, M., Muir, C. E., Poesch, M., & Shin, J. (2023). Physicochemical, particulate matter, temperature, and hydrological datasets collected from climate-threatened glacial river headwaters on the eastern slopes of the Canadian Rocky Mountains (2019-2021) [dataset]. *PANGAEA*. https://doi.org/10.1594/PANGAEA.963863

Serbu, J. A., St. Louis, V. L., Emmerton, C. A., Tank, S. E., Criscitiello, A. S., Silins, U., Bhatia, M. P., Cavaco, M. A., Christenson, C., Cooke, C. A., Drapeau, H. F., Enns, S. J. A., Flett, J. E., Holland, K. M., Lavallee-Whiffen, J., Ma, M., Muir, C. E., Poesch, M., & Shin, J.

https://doi.org/10.5194/egusphere-2025-5020
Preprint. Discussion started: 16 October 2025

(2024). A comprehensive biogeochemical assessment of climate-threatened glacial river headwaters on the eastern slopes of the Canadian Rocky Mountains. *Journal of Geophysical Research: Biogeosciences*, *129*(1), e2023JG007745. https://doi.org/10.1029/2023JG007745

Serbu, J. A., Tank, S. E., Peucker-Ehrenbrink, B., & St. Louis, V. L. (2024). Weathering dataset collected from climate-threatened glacial river headwaters on the eastern slopes of the Canadian Rocky Mountains (2019-2021). *PANGAEA*. https://doi.org/10.1594/PANGAEA.972842

Sharp, M., Creaser, R. A., & Skidmore, M. (2002). Strontium isotope composition of runoff from a glaciated carbonate terrain. *Geochimica et Cosmochimica Acta*, *66*(4), 595–614. https://doi.org/10.1016/S0016-7037(01)00798-0

Sharp, M., Tranter, M., Brown, G. H., & Skidmore, M. (1995). Rates of chemical denudation and CO_2 drawdown in a glacier-covered alpine catchment. *Geology*, *23*(1), 61. https://doi.org/10.1130/0091-7613(1995)023%253C0061:ROCDAC%253E2.3.CO;2

Spence, J., & Telmer, K. (2005). The role of sulfur in chemical weathering and atmospheric CO2 fluxes: Evidence from major ions, $\delta 13C_{DIC}$, and $\delta 34S_{SO4}$ in rivers of the Canadian Cordillera. *Geochimica et Cosmochimica Acta*, *69*(23), 5441–5458. https://doi.org/10.1016/j.gca.2005.07.011

St. Pierre, K. A., St. Louis, V. L., Schiff, S. L., Lehnherr, I., Dainard, P. G., Gardner, A. S., Aukes, P. J. K., & Sharp, M. J. (2019). Proglacial freshwaters are significant and previously unrecognized sinks of atmospheric CO_2. *Proceedings of the National Academy of Sciences*, *116*(36), 17690–17695. https://doi.org/10.1073/pnas.1904241116

https://doi.org/10.5194/egusphere-2025-5020
Preprint. Discussion started: 16 October 2025

Stevenson, E. I., Aciego, S. M., Chutcharavan, P., Parkinson, I. J., Burton, K. W., Blakowski, M. A., & Arendt, C. A. (2016). Insights into combined radiogenic and stable strontium isotopes as tracers for weathering processes in subglacial environments. *Chemical Geology*, *429*, 33–43. https://doi.org/10.1016/j.chemgeo.2016.03.008

Talling, J. F. (2010). Potassium—A Non-Limiting Nutrient in Fresh Waters? *Freshwater Reviews*, *3*(2), 97–104. https://doi.org/10.1608/FRJ-3.2.1

Torres, M. A., Moosdorf, N., Hartmann, J., Adkins, J. F., & West, A. J. (2017). Glacial weathering, sulfide oxidation, and global carbon cycle feedbacks. *Proceedings of the National Academy of Sciences*, *114*(33), 8716–8721. https://doi.org/10.1073/pnas.1702953114

Tranter, M., Sharp, M. J., Lamb, H. R., Brown, G. H., Hubbard, B. P., & Willis, I. C. (2002). Geochemical weathering at the bed of Haut Glacier d'Arolla, Switzerland—A new model. *Hydrological Processes*, *16*(5), 959–993. https://doi.org/10.1002/hyp.309

Tranter, M., & Wadham, J. L. (2014). Geochemical Weathering in Glacial and Proglacial Environments. In *Treatise on Geochemistry* (pp. 157–173). Elsevier. https://doi.org/10.1016/B978-0-08-095975-7.00505-2

Ulseth, A. J., Hall, R. O., Boix Canadell, M., Madinger, H. L., Niayifar, A., & Battin, T. J. (2019). Distinct air–water gas exchange regimes in low- and high-energy streams. *Nature Geoscience*, *12*(4), 259–263. https://doi.org/10.1038/s41561-019-0324-8

Urey, H. C. (1952). On the early chemical history of the Earth and the origin of life. *Proceedings of the National Academy of Sciences*, *38*(4), 351–363. https://doi.org/10.1073/pnas.38.4.351

https://doi.org/10.5194/egusphere-2025-5020
Preprint. Discussion started: 16 October 2025

Urra, A., Wadham, J., Hawkings, J. R., Telling, J., Hatton, J. E., Yde, J. C., Hasholt, B., Van As, D., Bhatia, M. P., & Nienow, P. (2019). Weathering dynamics under contrasting Greenland Ice Sheet catchments. *Frontiers in Earth Science*, *7*, 299. https://doi.org/10.3389/feart.2019.00299

U.S. EPA. (1993). Method 300.1: Determination of anions in drinking water by ion chromatography. In *Methods for the Determination of Organic and Inorganic Compounds in Drinking Water (EPA 815/R-00-014)*.

U.S. EPA. (1994). *Method 200.7, Revision 4.4: Determination of metals and trace elements in water and wastes by Inductively Coupled Plasma-Atomic Emission Spectrometry (ICP-AES)*.

Viers, J., Oliva, P., Dandurand, J.-L., Dupré, B., & Gaillardet, J. (2007). Chemical Weathering Rates, CO_2 Consumption, and Control Parameters Deduced from the Chemical Composition of Rivers. In *Treatise on Geochemistry* (2nd ed.).

Voss, B. M., Eglinton, T. I., Peucker-Ehrenbrink, B., Galy, V., Lang, S. Q., McIntyre, C., Spencer, R. G. M., Bulygina, E., Wang, Z. A., & Guay, K. A. (2023). Isotopic evidence for sources of dissolved carbon and the role of organic matter respiration in the Fraser River basin, Canada. *Biogeochemistry*, *164*(1), 207–228. https://doi.org/10.1007/s10533-022-00945-5

Voss, B. M., Peucker-Ehrenbrink, B., Eglinton, T. I., Fiske, G., Wang, Z. A., Hoering, K. A., Montluçon, D. B., LeCroy, C., Pal, S., Marsh, S., Gillies, S. L., Janmaat, A., Bennett, M., Downey, B., Fanslau, J., Fraser, H., Macklam-Harron, G., Martinec, M., & Wiebe, B. (2014). Tracing river chemistry in space and time: Dissolved inorganic constituents of the

https://doi.org/10.5194/egusphere-2025-5020
Preprint. Discussion started: 16 October 2025

Fraser River, Canada. *Geochimica et Cosmochimica Acta*, *124*, 283–308. https://doi.org/10.1016/j.gca.2013.09.006

Walker, J. C. G., Hays, P. B., & Kasting, J. F. (1981). A negative feedback mechanism for the long-term stabilization of Earth's surface temperature. *Journal of Geophysical Research: Oceans*, *86*(C10), 9776–9782. https://doi.org/10.1029/JC086iC10p09776

Wang, Z. A., Lawson, G. L., Pilskaln, C. H., & Maas, A. E. (2017). Seasonal controls of aragonite saturation states in the G ulf of M aine. *Journal of Geophysical Research: Oceans*, *122*(1), 372–389. https://doi.org/10.1002/2016JC012373

Wankiewicz, P. M. (1979). *Sedimentation in Sunwapta Lake, Jasper National Park, Alberta* [MSc]. University of Alberta.

Wanninkhof, R. (2014). Relationship between wind speed and gas exchange over the ocean revisited. *Limnology and Oceanography: Methods*, *12*(6), 351–362. https://doi.org/10.4319/lom.2014.12.351

Water Survey of Canada. (2021). *National Water Data Archive: HYDAT*. https://www.canada.ca/en/environment-climate-change/services/water-overview/quantity/monitoring/survey/data-products-services/national-archive-hydat.html

Zemp, M., Huss, M., Thibert, E., Eckert, N., McNabb, R., Huber, J., Barandun, M., Machguth, H., Nussbaumer, S. U., Gärtner-Roer, I., Thomson, L., Paul, F., Maussion, F., Kutuzov, S., & Cogley, J. G. (2019). Global glacier mass changes and their contributions to sea-level rise from 1961 to 2016. *Nature*, *568*(7752), 382–386. https://doi.org/10.1038/s41586-019-1071-0

https://doi.org/10.5194/egusphere-2025-5020
Preprint. Discussion started: 16 October 2025

Zolkos, S., Tank, S. E., & Kokelj, S. V. (2018). Mineral Weathering and the Permafrost Carbon-Climate Feedback. *Geophysical Research Letters*, *45*(18), 9623–9632. https://doi.org/10.1029/2018GL078748